

# TOI-2015 b: A sub-Neptune in strong gravitational interaction with an outer non-transiting planet

K. Barkaoui<sup>1,2,3,\*</sup>, J. Korth<sup>4</sup>, E. Gaidos<sup>5,6</sup>, E. Agol<sup>7,8</sup>, H. Parviainen<sup>9,3</sup>, F. J. Pozuelos<sup>10</sup>, E. Palle<sup>3,9</sup>, N. Narita<sup>12,13,3</sup>, S. Grimm<sup>15,16</sup>, M. Brady<sup>17</sup>, J. L. Bean<sup>17</sup>, G. Morello<sup>10,11</sup>, B. V. Rackham<sup>2,18</sup>, A. J. Burgasser<sup>33</sup>, V. Van Grootel<sup>19</sup>, B. Rojas-Ayala<sup>20</sup>, A. Seifahrt<sup>21</sup>, E. Marfil<sup>22</sup>, V. M. Passegger<sup>23,3,9,24</sup>, M. Stalport<sup>19</sup>, M. Gillon<sup>1</sup>, K. A. Collins<sup>26</sup>, A. Shporer<sup>18</sup>, S. Giacalone<sup>28</sup>, S. Yalçinkaya<sup>29,30,1</sup>, E. Ducrot<sup>25,31</sup>, M. Timmermans<sup>1</sup>, A. H. M. J. Triaud<sup>32</sup>, J. de Wit<sup>2</sup>, A. Soubkiou<sup>25</sup>, C. N. Watkins<sup>26</sup>, C. Aganze<sup>27</sup>, R. Alonso<sup>3,9</sup>, P. J. Amado<sup>10</sup>, R. Basant<sup>17</sup>, Ö. Baştürk<sup>29,30</sup>, Z. Benkhaldoun<sup>25</sup>, A. Burdanov<sup>2</sup>, Y. Calatayud-Borras<sup>3,9</sup>, J. Chouqar<sup>25</sup>, D. M. Conti<sup>34</sup>, K. I. Collins<sup>35</sup>, F. Davoudi<sup>1</sup>, L. Delrez<sup>1,19</sup>, C. D. Dressing<sup>36</sup>, J. de Leon<sup>37</sup>, M. Dévora-Pajares<sup>38</sup>, B. O. Demory<sup>39</sup>, G. Dransfield<sup>32</sup>, E. Esparza-Borges<sup>3,9</sup>, G. Fernández-Rodríguez<sup>3,9</sup>, I. Fukuda<sup>37</sup>, A. Fukui<sup>12,3</sup>, P. P. M. Gallardo<sup>3,9</sup>, L. García<sup>40,1</sup>, N. A. García<sup>3,9</sup>, M. Ghachoui<sup>25,1</sup>, S. Geraldía-González<sup>3,9</sup>, Y. Gómez Maqueo Chew<sup>41</sup>, J. González-Rodríguez<sup>3,9</sup>, M. N. Günther<sup>42</sup>, Y. Hayashi<sup>37</sup>, K. Horne<sup>43</sup>, M. J. Hooton<sup>44</sup>, C. C. Hsu<sup>45</sup>, K. Ikuta<sup>37</sup>, K. Isogai<sup>46,37</sup>, E. Jehin<sup>19</sup>, J. M. Jenkins<sup>47</sup>, K. Kawauchi<sup>48</sup>, T. Kagetani<sup>37</sup>, Y. Kawai<sup>37</sup>, D. Kasper<sup>17</sup>, J. F. Kielkopf<sup>49</sup>, P. Klagyivik<sup>50</sup>, G. Lacedelli<sup>3</sup>, D. W. Latham<sup>26</sup>, F. Libotte<sup>3,51,52</sup>, R. Luque<sup>17,25</sup>, J. H. Livingston<sup>13,53,54</sup>, L. Mancini<sup>55,56,57</sup>, B. Massey<sup>58</sup>, M. Mori<sup>13,53</sup>, S. Muñoz Torres<sup>3,9</sup>, F. Murgas<sup>3,9</sup>, P. Niraula<sup>2</sup>, J. Orell-Miquel<sup>3,9</sup>, David Rapetti<sup>47,14</sup>, R. Rebolo-López<sup>3,9</sup>, G. Ricker<sup>18</sup>, R. Papini<sup>59</sup>, P. P. Pedersen<sup>44,60</sup>, A. Peláez-Torres<sup>10</sup>, J. A. Pérez-Prieto<sup>3</sup>, E. Poultourtzidis<sup>3,61</sup>, P. M. Rodriguez<sup>3,9</sup>, D. Queloz<sup>44,60</sup>, A. B. Savel<sup>62</sup>, N. Schanche<sup>39</sup>, M. Sánchez-Benavente<sup>3,9</sup>, L. Sibbald<sup>63</sup>, R. Sefako<sup>64</sup>, S. Sohy<sup>19</sup>, A. Sota<sup>10</sup>, R. P. Schwarz<sup>26</sup>, S. Seager<sup>33,9,62</sup>, D. Sebastian<sup>32</sup>, J. Southworth<sup>65</sup>, M. Stangret<sup>66</sup>, G. Stefánsson<sup>67</sup>, J. Stürmer<sup>68</sup>, G. Srdic<sup>69</sup>, S. J. Thompson<sup>44</sup>, Y. Terada<sup>70,71</sup>, R. Vanderspek<sup>18</sup>, G. Wang<sup>72</sup>, N. Watanabe<sup>37</sup>, F. P. Wilkin<sup>73</sup>, J. Winn<sup>74</sup>, R. D. Wells<sup>39</sup>, C. Ziegler<sup>75</sup>, and S. Zúñiga-Fernández<sup>1</sup>

(Affiliations can be found after the references)

Received 7 November 2024 / Accepted 10 February 2025

## ABSTRACT

TOI-2015 is a known exoplanetary system around an M4 dwarf star, consisting of a transiting sub-Neptune planet in a 3.35-day orbital period, TOI-2015 b, accompanied by a non-transiting companion, TOI-2015 c. High-precision radial-velocity measurements were taken with the MAROON-X spectrograph, and high-precision photometric data were collected, primarily using the SPECULOOS, MUSCAT, TRAPPIST and LCOGT networks. We collected 63 transit light curves and 49 different transit epochs for TOI-2015 b. We re-characterized the target star by combining optical spectra obtained by the MAROON-X, Shane/KAST and IRTF/Spex spectrographs, Bayesian model averaging (BMA) and spectral energy distribution (SED) analysis. The TOI-2015 host star is a  $K = 10.3$  mag M4-type dwarf with a subsolar metallicity of  $[Fe/H] = -0.31 \pm 0.16$ , and an effective temperature of  $T_{eff} \approx 3200$  K. Our photodynamical analysis of the system strongly favors the 5:3 mean-motion resonance and in this scenario the planet b (TOI-2015 b) has an orbital period of  $P_b = 3.34$  days, a mass of  $M_p = 9.02_{-0.36}^{+0.32} M_{\oplus}$ , and a radius of  $R_p = 3.309_{-0.011}^{+0.013} R_{\oplus}$ , resulting in a density of  $\rho_p = 0.25 \pm 0.01 \rho_{\oplus} = 1.40 \pm 0.06 \text{ g cm}^{-3}$ ; this is indicative of a Neptune-like composition. Its transits exhibit large (> 1 hr) timing variations characteristic of an outer perturber in the system. We performed a global analysis of the high-resolution radial-velocity measurements, the photometric data, and the TTVs, and inferred that TOI-2015 hosts a second planet, TOI-2015 c, in a non-transiting configuration. Our analysis places it near a 5:3 resonance with an orbital period of  $P_c = 5.583$  days and a mass of  $M_p = 8.91_{-0.40}^{+0.38} M_{\oplus}$ . The dynamical configuration of TOI-2015 b and TOI-2015 c can be used to constrain the system's planetary formation and migration history. Based on the mass-radius composition models, TOI-2015 b is a water-rich or rocky planet with a hydrogen-helium envelope. Moreover, TOI-2015 b has a high transmission-spectroscopic metric (TSM= 149), making it a favorable target for future transmission spectroscopic observations with the *JWST* to constrain the atmospheric composition of the planet. Such observations would also help to break the degeneracies in theoretical models of the planet's interior structure.

**Key words.** planets and satellites: detection – planets and satellites: formation – stars: individual: TOI-2015

## 1. Introduction

The Milky Way is dominated by M dwarf stars (Henry 1994; Henry et al. 2006), which are intriguing targets for searching

for and characterizing small planets. M-dwarf systems offer a unique opportunity to explore their physical properties thanks to their small sizes and low masses. The relatively small size of the host star leads to deep transits, and large radial-velocity (RV) and TTV signals. This allowed us to explore the interior structure and atmospheric composition of the planets, by measuring their sizes and masses (e.g. Dorn et al. 2017).

\* Corresponding author: [khalid.barkaoui@uliege.be](mailto:khalid.barkaoui@uliege.be)

\*\* Paris Region Fellow, Marie Skłodowska-Curie Action.

\*\*\* NHFP Sagan Fellow.

Transit timing variations (TTVs, [Agol et al. 2005](#); [Holman & Murray 2005](#)) can be used to search for additional non-transiting exoplanets and to estimate their physical parameters (orbital parameters and planetary masses) thanks to the planet's gravitational perturbation. The TTV amplitude depends on the mass of the perturbing planet as well as the orbital eccentricities and longitudes of the pericenter of each planet (see, e.g., [Deck & Agol 2016](#)). Transiting planets in a multi-planet system with strong gravitational influences offer us an excellent opportunity to explore the interior composition of exoplanets. Moreover, the combination of planet sizes measured from transit depths and masses measured from TTVs and RVs yields densities and clues to the interior composition of planets. Near-resonant multi-planet systems, which exhibit nearly exact integer ratios of their orbital periods, offer special opportunities to derive the formation and evolution mechanisms of the systems. Currently, there are about 374 planetary systems that show TTVs, only  $\sim 20$  of which orbit M dwarfs, including the well-characterized TRAPPIST-1 system, a resonant system with seven transiting rocky worlds orbiting a nearby late M-dwarf star ([Gillon et al. 2016, 2017](#); [Agol et al. 2021a](#)).

TOI-2015 was confirmed by [Jones et al. \(2024\)](#) using the Transiting Exoplanet Survey Satellite data, and WIRO-2.3m, and RBO-0.6m and ARC-3.5m photometric data and RV measurements collected with the Habitable-zone Planet Finder Spectrograph. The analysis [Jones et al. \(2024\)](#) placed the non-transiting planet TOI-2015 c within near 2:1 resonance. The authors found that TOI-2015 b has a radius of  $R_b = 3.37^{+0.15}_{-0.20} R_{\oplus}$  and a mass of  $M_b = 13.3^{+4.7}_{-4.5} M_{\oplus}$ , and TOI-2015 c has a mass of  $M_c = 6.8^{+3.5}_{-2.3} M_{\oplus}$ . However, other possible two-planet solutions –such as 3:2 and 4:3 near-resonances– could not be conclusively excluded without complementary photometric and RV observations. In this paper, we extended their analysis including further period ratios (5:3 and 5:2 resonances) to justify and set the stage for the justification for the paper. In this context, we present a new photodynamical analysis of the TOI-2015 system using *TESS* data, new ground-based photometric data and radial velocity measurements collected with the MAROON-X spectrograph. We collected a total of 63 transit light curves of the transiting planet TOI-2015 b and 28 radial velocity measurements. This enabled us to enhance the accuracy of the physical parameters of both planets, and better constrain composition and origin.

The paper is structured as follows. Section 2 describes the *TESS* and ground-based follow-up (photometric, spectroscopic, and high-angular-resolution imaging) observations used to characterize the system. Section 3 describes the stellar characterization of TOI-2015 using spectral energy distributions (SEDs), stellar evolution models, spectroscopic observations, and spectral and photometric fitting using Bayesian model averaging (BMA). The validation of the planet transit signals in the photometric data is presented in Section 4. A photodynamical analysis of photometric data, RVs, and TTV measurements is presented in Section 5, and an independent TTV analysis is presented in Section 6, allowing us to characterize the system. The planet searches and detection limits are presented in Section 7. Finally, our discussion and conclusions are presented in Sections 8 and 9, respectively.

## 2. Observation and data reduction

### 2.1. *TESS* photometry

The host star TIC 368287008 (TOI-2015) was observed by *TESS* ([Ricker et al. 2015](#)) in Sectors 24, 51, and 78 for 27 days each with 2-min cadence. Observation dates are presented in Table B.1.

The Sector 51 campaign started on 2022 April 22 and ended on 2022 May 18. The two gaps during Sector 51 were caused by scattered light and high background levels<sup>1</sup>, and we ignored them. The Sector 78 campaign started on 2024 April 23 and ended on 2024 May 21. The target was observed in Camera 1 CCD 3. The first gap in the data is due to the Safe Hold mode of the spacecraft, while the second gap is due to the scattered light as Camera 1 was too close to Earth between  $\text{BJD}_{\text{TDB}} = 2460444$  and  $\text{BJD}_{\text{TDB}} = 2460449$  (see *TESS* observation report)<sup>2</sup>.

To analyze the *TESS* photometric data, we used the presearch data conditioning light curves (PCD-SAP) extracted from the Mikulski Archive for Space Telescopes ([Stumpe et al. 2012](#); [Smith et al. 2012](#); [Stumpe et al. 2014](#)) constructed by the *TESS* Science Processing Operations Center (SPOC, [Jenkins et al. 2016](#)) at Ames Research Center. PDC-SAP light curves have been corrected for any crowding and instrument systematics effects. The signature of TOI-2015 b was first detected by the *TESS* SPOC pipeline in Sectors 24 and 51. The TOI-2015 FOV including the location of nearby Gaia DR3 sources ([Gaia Collaboration 2021](#)) and photometric apertures are presented in Figure 1. *TESS* transit light curves for TOI-2015 b are presented in Figure 2.

### 2.2. Ground-based photometric follow-up

We used the *TESS* Transit Finder tool to schedule the photometric observations. It is a customized version of the Tapir software package ([Jensen 2013](#)). These are summarized in the following sections, and the resulting transit light curves are presented in Figure 3. The observation log is presented in Table C.1. The transit timing measurements are presented in Table D.1.

#### 2.2.1. SPECULOOS-North

We used SPECULOOS-North/Artemis (Search for habitable Planets EClipsing ULtra-cOOI Stars, [Burdanov et al. 2022](#)) at Teide observatory to observe the transits of TOI-2015 b. Artemis is a 1.0-m Ritchey-Chrétien telescope equipped with a thermoelectrically cooled 2K×2K Andor iKon-L BEX2-DD CCD camera with a pixel scale of 0.35''/pixel and a total field-of-view (FOV) of 12' × 12'. SPECULOOS-North is a sibling of the SPECULOOS-South ([Jehin et al. 2018](#); [Delrez et al. 2018](#); [Sebastian et al. 2021](#)) and SAINT-EX (Search And characterIsatioN of Transiting EXoplanets, [Demory et al. 2020](#)) telescopes. We observed a total of 15 (full and partial) transits in the  $I + z$  filter with an exposure time of 10s. The observation dates are presented in Table C.1. Data calibration and photometric extraction were performed using the PROSE<sup>3</sup> pipeline ([Garcia et al. 2022](#)).

#### 2.2.2. SAINT-EX

We observed one full transit of TOI-2015 b with SAINT-EX on UT 2022 June 19 in the  $I + z'$  filter with an exposure time of 10 s. SAINT-EX ([Demory et al. 2020](#)) is a 1.0-m  $f/8$  Ritchey-Chrétien telescope located at the Sierra de San Pedro Mártir in Baja California, México. SAINT-EX is equipped with a thermoelectrically cooled 2K×2K Andor iKon-L CCD camera, with a

<sup>1</sup> TESS Report for Sector 51: [tess\\_sector\\_51\\_drn74\\_v02.pdf](#)

<sup>2</sup> TESS Report for Sector 78: [tess\\_sector\\_78\\_drn110\\_v01.pdf](#)

<sup>3</sup> Prose: <https://github.com/lgracia/prose>

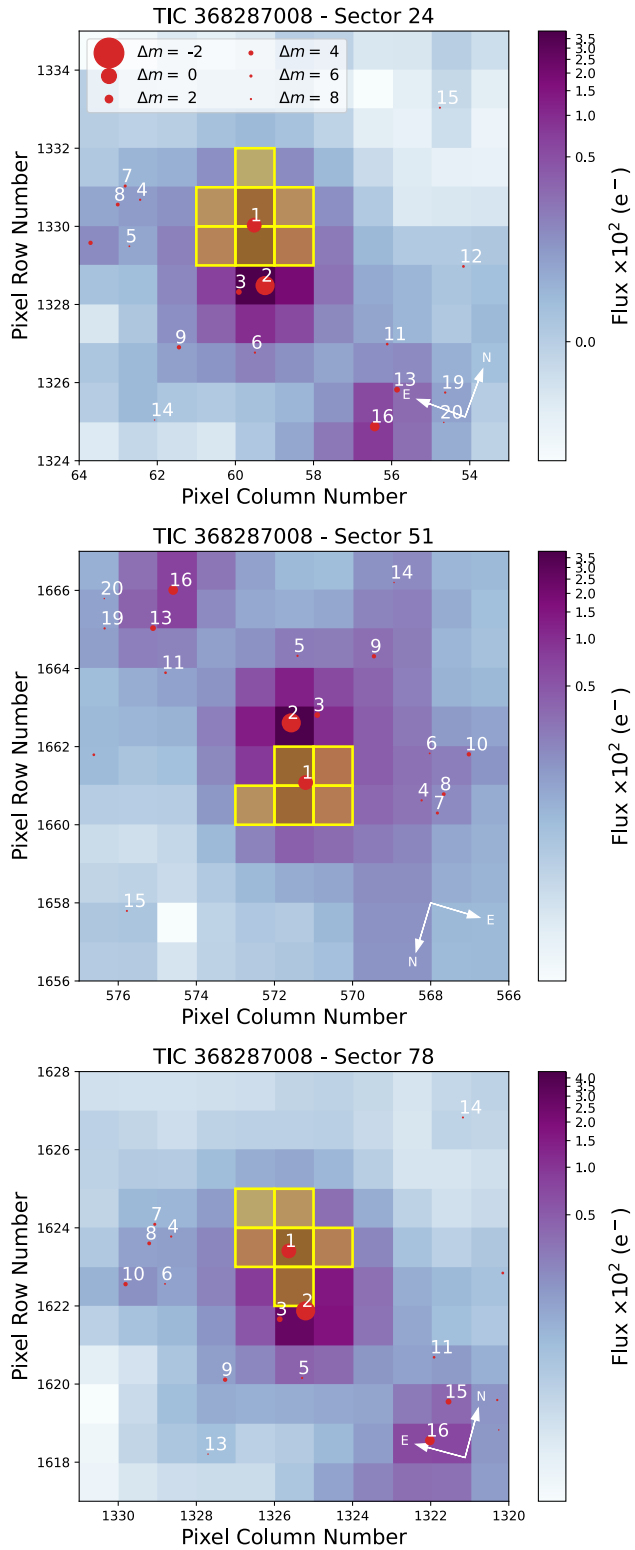


**Fig. 1.** *TESS* target pixel file images of TOI-2015 observed in Sectors 24 (top), 51 (middle), and 78 (bottom) made by `tpfplotter` (Aller et al. 2020). Red dots show the location of Gaia DR3 sources, and the yellow shaded regions show the photometric apertures used to extract the photometric measurements.

FOV of  $12' \times 12'$  and a pixel scale of  $0.35''/\text{pixel}$ . The data calibration and photometric extraction were performed using the PROSE pipeline (Garcia et al. 2022).

### 2.2.3. TRAPPIST-South

One full transit was observed with the TRAPPIST-South (TRAnsiting Planets and PlanetesImals Small Telescope, Jehin et al. 2011; Gillon et al. 2011) telescope on UT 2022 May 29 in the  $I + z'$  filter with an exposure time of 55 s. It is a 60-cm Ritchey-Chrétien telescope located at ESO-La Silla Observatory in Chile, which is the twin of TRAPPIST-North. It is equipped with a  $2\text{K} \times 2\text{K}$  FLI Proline CCD camera with a FOV of  $22' \times 22'$  and a pixel scale of  $0.65''/\text{pixel}$ . The data calibration and photometric extraction were performed using the PROSE pipeline (Garcia et al. 2022).

### 2.2.4. TRAPPIST-North

TRAPPIST-North (Barkaoui et al. 2019) observed three transits of TOI-2015 b in the  $I + z'$  filter with an exposure time of 50s. The telescope is a 60-cm Ritchey-Chrétien telescope located at Oukaimeden Observatory, and it is equipped with a thermoelectrically cooled  $2\text{K} \times 2\text{K}$  Andor iKon-L BEX2-DD CCD camera with a pixel scale of  $0.6''$ , resulting in a FOV of  $20' \times 20'$ . The data calibration and photometric extraction were performed using the PROSE pipeline (Garcia et al. 2022). The observation dates are given in Table C.1.

### 2.2.5. MuSCAT

We observed one full transit of TOI-2015 b on UT 2022 May 06 with MuSCAT, a simultaneous multi-band camera installed on the 188-cm telescope in Okayama, Japan (Narita et al. 2015). MuSCAT has three optical channels of  $g'$ ,  $r'$ , and  $z_s$ -bands with a pixel scale of  $0.358''/\text{pixel}$  and  $6'.1 \times 6'.1$  field of view. The reduction and the aperture photometry were conducted by the custom pipeline described in Fukui et al. (2011). The optimal aperture radius and set of comparison stars were selected for each band to minimize the scatter in the light curves.

### 2.2.6. MuSCAT2

Two full transits of TOI-2015 b were observed on UT 2022 May 19 and 2022 May 29 with the MuSCAT2 multicolor imager (Narita et al. 2019) mounted on the 1.52m-Telescopio Carlos Sánchez (TCS) at the Teide Observatory in Tenerife (Canary Islands, Spain). Both transits were carried out simultaneously in the Sloan- $g'$ ,  $-r'$ ,  $-i'$ , and  $z_s$ . The photometric measurements were extracted using an uncontaminated photometric aperture (see Table C.1). The data calibration and photometric analysis were performed using the MuSCAT2 photometry pipeline (Parviaainen et al. 2020).

### 2.2.7. LCOGT-2m0/MuSCAT3

We used the Las Cumbres Observatory Global Telescope (LCOGT; Brown et al. 2013) 2.0-m Faulkes Telescope North at Haleakala Observatory in Hawaii to observe a total of six transits of TOI-2015 b simultaneously in Sloan- $g'$ ,  $-r'$ ,  $-i'$ , and  $z_s$  filters. The observation dates are given in Table C.1. The telescope is equipped with the MuSCAT3 multiband imager (Narita et al. 2020). The data calibration was performed using the standard LCOGT BANZAI pipeline (McCully et al. 2018), and photometric measurements were extracted using AstroImageJ<sup>4</sup> (Collins et al. 2017).

<sup>4</sup> AstroImageJ: <https://www.astro.louisville.edu/software/astroimagej/>

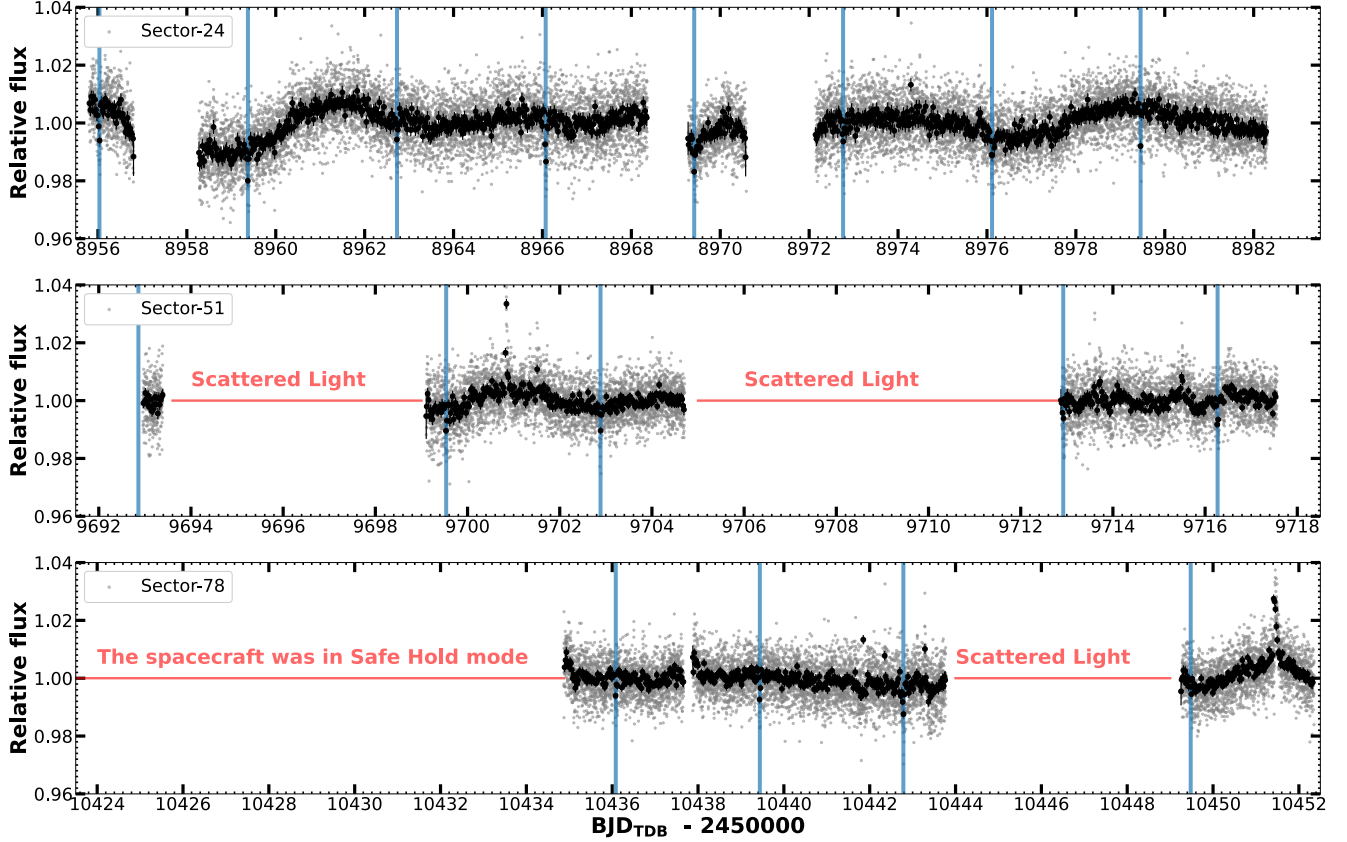


**Fig. 2.** TESS PDC-SAP flux extracted from 2-min cadence data of TOI-2015. The target was observed in Sectors 24 (top), 51 (middle), and 78 (bottom). The light gray points show the 2-min cadence data, and the black points show the flux in 30-min bins. The transit locations of TOI-2015 b are shown with vertical blue lines.

#### 2.2.8. LCOGT-1.0-m

We used the Las Cumbres Observatory Global Telescope (LCOGT; [Brown et al. 2013](#)) 1.0-m network to observe a total of 15 transits (full and partial) of TOI-2015 b in the Sloan-*i'* filter. The observation dates are given in Table C.1. Each telescope is equipped with  $4096 \times 4096$  SINISTRO Cameras, with an image scale of  $0.389''$  per pixel and a total FOV of  $26' \times 26'$ . The data calibration was performed using the standard LCOGT BANZAI pipeline ([McCully et al. 2018](#)) and photometric measurements were extracted using AstroImageJ ([Collins et al. 2017](#)).

#### 2.2.9. OSN-1.5m

We observed one partial transit of TOI-2015 b on UT 2022 June 25 in the Johnson-Cousin *I* filter using the T150 at the Sierra Nevada Observatory in Granada (Spain). The T150 is equipped with a  $2K \times 2K$  Andor iKon-L BEX2DD CCD camera with a pixel scale of  $0.232''$ , resulting in a FOV of  $7.9' \times 7.9'$ . The data calibration and photometric extraction were performed using AstroImageJ ([Collins et al. 2017](#)).

#### 2.2.10. IAC80

We observed a full transit of TOI-2015 b on UT 2024 May 09 in the Sloan-*r'* filter using the IAC80 telescope located at Teide Observatory in Tenerife (Canary Islands, Spain). The IAC80 is an 82 cm telescope equipped with a  $4K \times 4K$  CCD camera with a plate scale of  $0.32''/\text{pixel}$ , resulting in a FOV of  $21.98' \times 22.06'$ .

The data calibration and photometric extraction were performed using AstroImageJ ([Collins et al. 2017](#)).

#### 2.2.11. T100

One full transit was observed with the 1-m Turkish telescope T100, located at the Türkiye National Observatories Bakırköy Campus at an altitude of 2500 meters on UT 2023 June 25. The telescope is equipped with a cryo-cooled SI 1100 CCD that has  $4096 \times 4096$  pixels, providing an effective field of view (FoV) of  $21' \times 21'$ . We used the CCD in  $2 \times 2$  binning mode to decrease the readout time from 45 s to 15 s. We slightly defocused the telescope to increase the precision ([Baştürk et al. 2015](#)) and observed without a filter, to capture all wavelengths of light and thus maximize the precision. Calibration of the raw images, aperture photometry with respect to an ensemble of comparison stars, and airmass detrending were performed using AstroImageJ.

#### 2.2.12. CAHA-1.23 m

One full transit of TOI-2015 b was observed on UT 2023 June 15 with the Zeiss 1.23 m telescope at the Observatory of Calar Alto in Spain. The telescope is equipped with an iKon-XL 230 camera, with  $4096 \times 4108$  pixels of size  $15 \mu\text{m}$ . The pixel scale is  $0.32 \text{ arcsec pixel}^{-1}$  and the FOV is  $21.4 \text{ arcmin} \times 21.5 \text{ arcmin}$ . The transit was monitored through the special uncoated GG-495 glass long-pass filter (transparent at  $>500 \text{ nm}$ ). Observations were performed by slightly defocusing the telescopes, in order to increase the photometric precision (e.g., [Southworth et al. 2012](#); [Mancini et al. 2013](#)), and using autoguiding. An exposure time

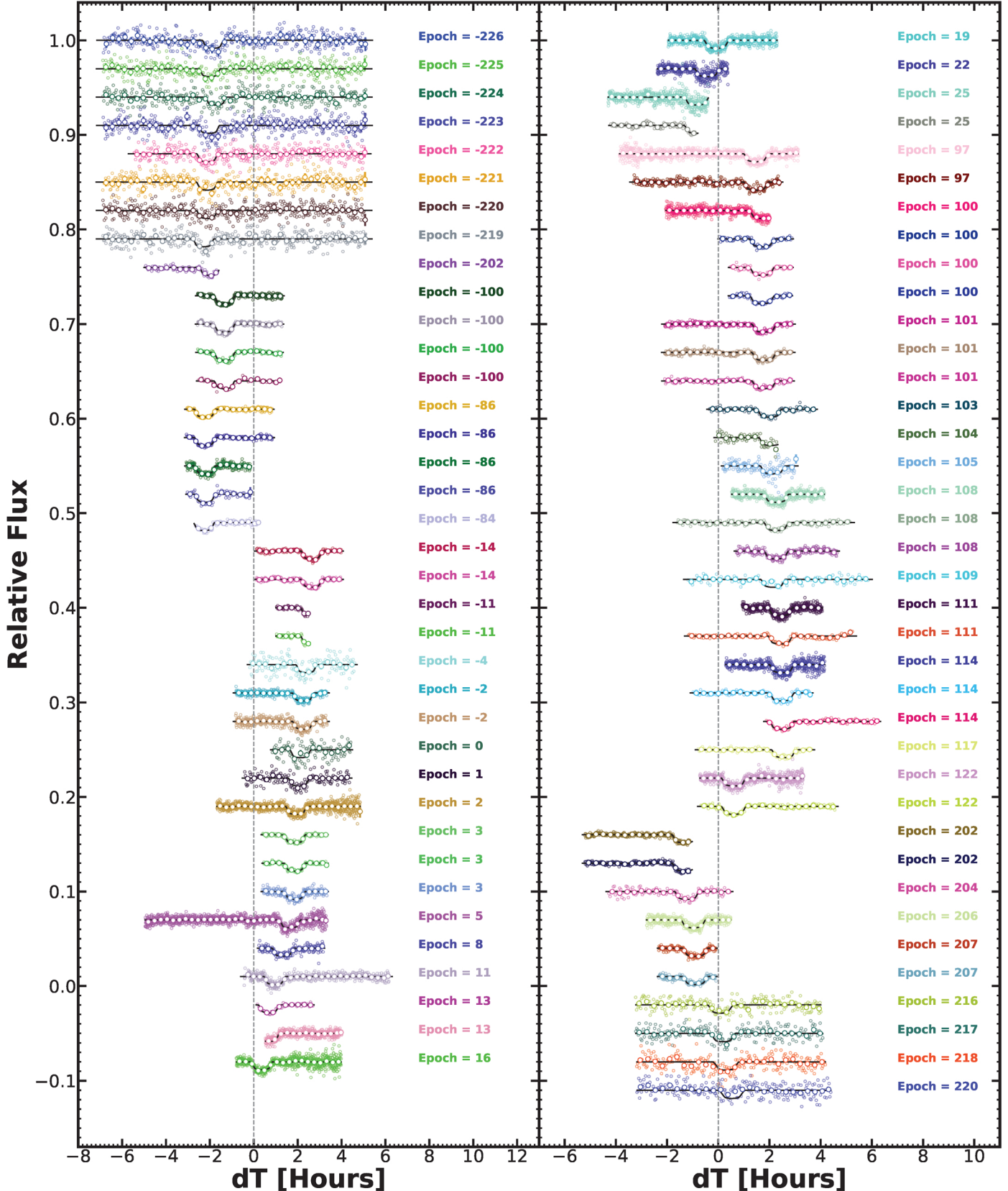


**Fig. 3.** *TESS* and ground-based transit light curves for TOI-2015 b, plotted with arbitrary vertical offsets for clarity. The colored data points show the relative flux and the black lines show the best-fitting transit model superimposed. The light curves are shifted along the x-axis according to the TTVs and along the y-axis for the visibility. The corresponding transit epoch is shown on the right of each transit light curve.

between 110 and 120 seconds was adopted. The science data were calibrated by adopting the same procedure as in [Mancini et al. \(2017\)](#). Standard aperture photometry was used to extract the light curves of the planetary transit. This was done by placing the usual three apertures on the target and on five good comparison stars and running the APER routine ([Southworth et al. 2010](#)). The sizes of the apertures were decided after several attempts, by selecting those with the lowest scatter when compared with a fit model. The resulting light curve was normalized to zero magnitude by a quadratic fit to the out-of-transit data versus the comparison stars.

### 2.3. Spectroscopy

#### 2.3.1. Spectroscopic follow-up using MAROON-X

We observed TOI-2015 15 times with the MAROON-X spectrograph ([Seifahrt et al. 2018, 2022](#)) on Gemini-North between UT 2021 April and UT 2023 July. MAROON-X is an extreme precision radial velocity (EPRV) spectrograph with a wavelength coverage suitable for M-dwarf observations. MAROON-X has two CCDs encompassing different wavelength ranges, with a “red” channel at 650–920 nm and a “blue” channel at 500–670 nm. Both of these CCDs were exposed simultaneously during an observation of TOI-2015, meaning that we have 15 red-channel RVs and 15 blue-channel RVs. As these two channels are independent of one another and encompass different wavelength ranges, we consider them to be two different instruments for the purposes of our analysis, as they may capture different chromatic stellar signals.

The MAROON-X data were reduced using a custom Python3 pipeline and tools developed for the CRIRES instrument ([Bean et al. 2010](#)). We calculated RVs from the reduced spectrum using a modified version of `serval` ([Zechmeister et al. 2020](#)) customized to work with MAROON-X data. `serval` calculates RVs by co-adding all of the available spectra for the target to produce a high-S/R template, which is then compared to each individual spectrum in order to calculate the relative RV shift.

Our data have exposure times ranging from 520 to 1800 s, with one exposure at 2400 s. In general, we found that the spectra with 520 s exposure times had very large RV errors due to the faint nature of the host star. We increased our exposure times later in the survey in order to improve the RV precision (and reduce time lost to telescope overhead). Overall, we have ten exposures with the longer exposure times. Two of the short exposures in the blue channel had  $\text{SNR} < 10$  and were thus not included in the `serval` results. Omitting the 520 s exposures, the red-channel spectra have a median SNR of 94 and a resulting median RV error of  $1.4 \text{ m s}^{-1}$ . The blue-channel spectra have a median SNR of 33 and a median RV error of  $3.1 \text{ m s}^{-1}$ . The resulting RV measurements and curve are presented in Table 1 and Figure 4.

#### 2.3.2. IRTF/SpeX spectroscopy

We collected a medium-resolution near-infrared spectrum of TOI-2015 with the SpeX spectrograph ([Rayner et al. 2003](#)) on the 3.2-m NASA Infrared Telescope Facility (IRTF) on UT 2022 April 19. Thin cirrus was present, and seeing was  $1''.0$ . Using the short-wavelength cross-dispersed (SXD) mode with the  $0.3'' \times 15''$  slit aligned to the parallactic angle, we gathered spectra covering  $0.80$ – $2.42 \mu\text{m}$  with a resolving power of  $R \sim 2000$ . Nodding in an ABBA pattern, we collected six exposures of  $114.9$  s each, totaling  $689.4$  s on source. We collected a

**Table 1.** Radial-velocity measurements for TOI-2015 obtained by MAROON-X in the “red” and “blue” channels.

BJD <sub>TDB</sub>	Red channel $\text{RV} \pm \sigma_{\text{RV}}$ (m/s)	Blue channel $\text{RV} \pm \sigma_{\text{RV}}$ (m/s)
2459332.94938	$-2.581 \pm 5.003$	$36.052 \pm 13.656$
2459333.95573	$-6.697 \pm 3.404$	$-16.506 \pm 8.681$
2459334.95363	$-15.835 \pm 3.113$	$-28.145 \pm 7.595$
2459358.94624	$4.576 \pm 6.018$	–
2459359.92272	$10.594 \pm 5.348$	–
2459361.92241	$-4.669 \pm 1.427$	$-5.860 \pm 3.417$
2459362.80767	$-6.133 \pm 1.153$	$-12.592 \pm 2.828$
2459363.87855	$7.915 \pm 1.514$	$6.392 \pm 3.623$
2459365.93460	$11.654 \pm 1.494$	$19.844 \pm 3.651$
2459367.91986	$-6.518 \pm 1.391$	$-7.968 \pm 3.255$
2459368.83965	$-10.798 \pm 1.239$	$-9.334 \pm 2.871$
2459368.91956	$-10.754 \pm 1.270$	$-9.599 \pm 2.950$
2459369.96677	$5.781 \pm 1.705$	$16.241 \pm 4.477$
2460127.91889	$20.109 \pm 1.351$	$26.724 \pm 2.611$
2460130.78194	$8.402 \pm 1.450$	$5.732 \pm 2.868$

standard set of SXD flat-field and arc-lamp exposures after the science observations, followed by a set of six, 3.7-s exposures of the A0 V star HD 140729 ( $V=6.1$ ). Data calibration was performed using `Spextool v4.1` ([Cushing et al. 2004](#)), following the instructions for standard usage in the `Spextool` user manual<sup>5</sup>. The final spectrum has a median S/R per pixel of 83 with peaks in the  $J$ ,  $H$ , and  $K$  bands of 108, 119, and 110, respectively, and an average of 2.7 pixels per resolution element.

#### 2.3.3. Shane/Kast optical spectroscopy

We observed TOI-2015 with the Kast double spectrograph ([Miller & Stone 1994](#)) mounted on the 3m Shane telescope at Lick Observatory on UT 2022 July 02. Conditions were mostly clear with scattered clouds and  $1''$  seeing. We used the  $1''$  slit aligned to the parallactic angle to obtain blue and red optical spectra split at  $5700 \text{ \AA}$  by the d57 dichroic and dispersed by the 600/4310 grism and 600/7500 grating, respectively, for a common resolution of  $\lambda/\Delta\lambda \approx 2000$ . We obtained a single 1200 s exposure in the blue channel and two 600 s exposures in the red channel at an average airmass of 1.07. The G2 V star HD 104385 ( $V = 8.57$ ) was observed immediately before TOI-2015 for telluric absorption calibration, and the spectrophotometric calibrator Feige 66 ([Hamuy et al. 1992, 1994](#)) was observed during the night for flux calibration. We obtained HeHgCd and HeNe-eArHg arc lamp exposures at the start of the night to wavelength calibrate our blue and red data, respectively; flat-field lamp exposures for pixel-response calibration were also obtained. Data were reduced using the `kastredux` code<sup>6</sup> using standard settings. We focused on our analysis on the higher quality red optical data which span  $6000$ – $9000 \text{ \AA}$  and have a median signal-to-noise ratio = 130 at  $7350 \text{ \AA}$ .

<sup>5</sup> Available at <http://irtfweb.ifa.hawaii.edu/~spex/observer/>

<sup>6</sup> <https://github.com/aburgasser/kastredux>

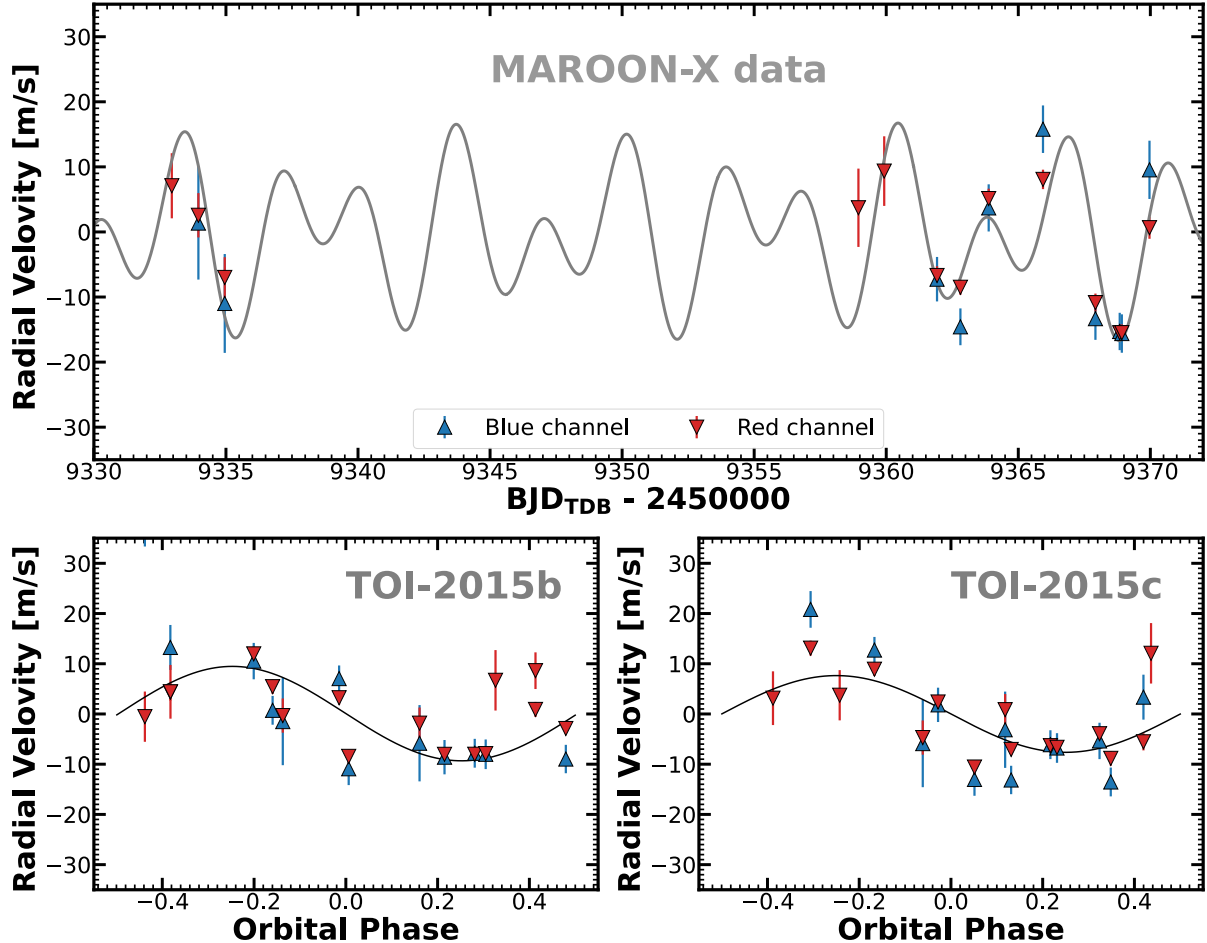


**Fig. 4.** Radial-velocity measurements in “red” (red triangles) and “blue” (blue triangles) channels with error bars) of the two-planets TOI-2015 b and TOI-2015 c collected with the MAROON-X spectrograph. The solid gray line shows the best-fit radial velocity data for the 5:3 scenario.

#### 2.4. High-resolution imaging

High-angular-resolution imaging is required to check for nearby sources that could contaminate the *TESS* photometry, resulting in an underestimated radius of the occulting object, or that can be the source of astrophysical false positives, such as blended eclipsing binaries.

##### 2.4.1. 4.1-m SOAR observations of TOI-2015

We searched for stellar companions to TOI-2015 using speckle imaging installed on the 4.1m Southern Astrophysical Research (SOAR) telescope (Tokovinin 2018) on UT 2021 April 25, observing in the Cousins-I filter, a similar bandpass to *TESS*. This observation was sensitive enough to detect a 4.2-mag fainter star at an angular distance of 1 arcsec from the target. Further details of the SOAR observations are available in Ziegler et al. (2020). Figure 5 shows the speckle auto-correlation functions and the  $5\sigma$  detection sensitivity. No nearby sources have been detected within 3'' of TOI-2015 in the SOAR data.

##### 2.4.2. 3.0 m-Shane observations of TOI-2015

We observed TOI-2015 with the ShARCS camera on the Shane 3.0-m telescope located at Lick Observatory (Kupke et al. 2012; Gavel et al. 2014; McGurk et al. 2014) on UT 2021 March 04.

Observations were taken with the Shane adaptive optics system in natural-guide-star mode to search for nearby unresolved stellar companions. Sequences of observations were collected using the  $K_s$  and  $J$  filters. The data reduction was performed using the publicly available SImMER<sup>7</sup> pipeline (Savel et al. 2020, 2022). No nearby stellar sources have been detected within detection limits (see Figure 5).

## 3. Stellar characterization

### 3.1. SED analysis and evolutionary models

As a first determination of the basic stellar parameters, we performed an analysis of the broadband SED of the star together with the *Gaia* DR3 parallax (with no systematic offset applied; see, e.g., Stassun & Torres 2021), in order to derive an empirical measurement of the stellar radius, following the procedures described in Stassun & Torres (2016); Stassun et al. (2017, 2018a). We pulled the  $JHK_s$  magnitudes from 2MASS, the W1–W3 magnitudes from *WISE*, the  $G_{\text{BP}}G_{\text{RP}}$  magnitudes from *Gaia*, and the  $zy$  magnitudes from *Pan-STARRS*. Together, the available photometry spans the full stellar SED over the 0.4–10  $\mu\text{m}$  wavelength range (see Figure 6).

<sup>7</sup> SImMER: <https://github.com/arjunsavel/SImMER>

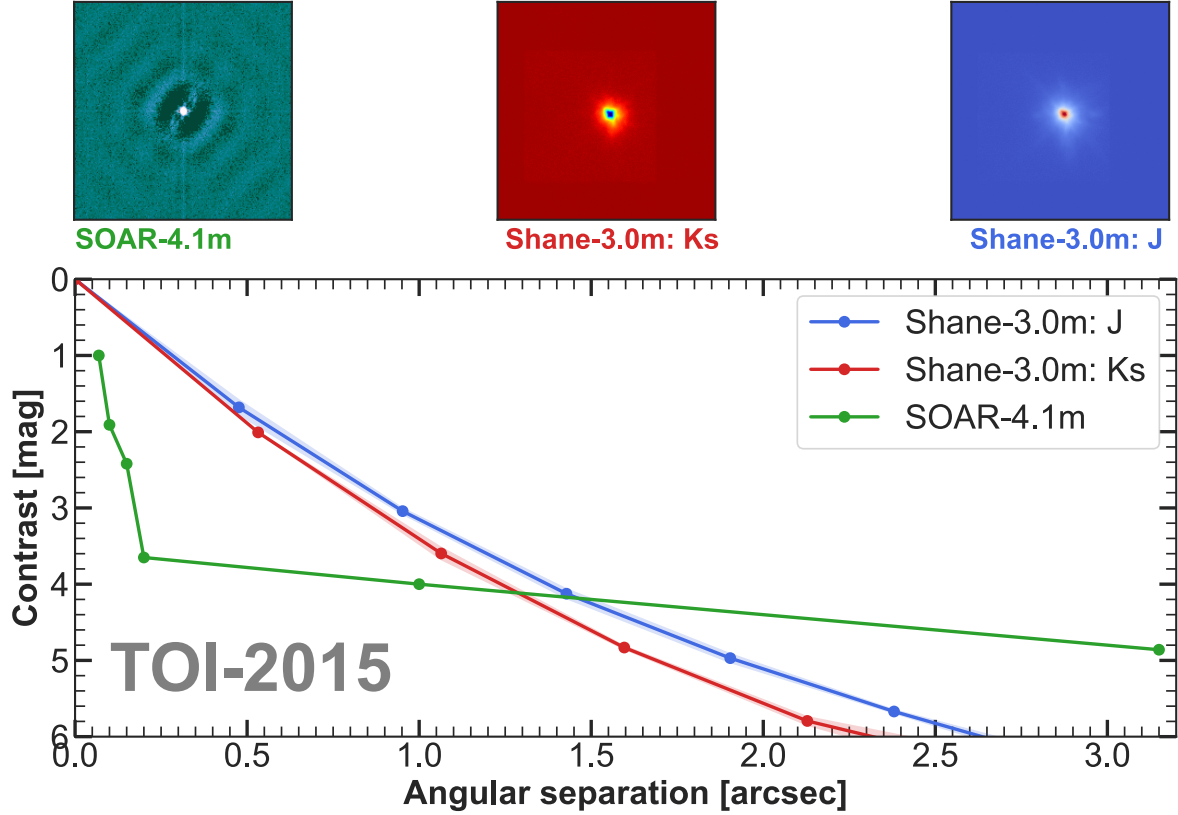


**Fig. 5.** High-angular-resolution imaging of TOI-2015 from 4.1-m SOAR telescope on UT 2021 April 25 in the  $K_s$  filter (green panel) and the 3.0-m SHANE telescope on UT 2021 March 04 in the  $K$  (red panel) and  $J$  (blue panel) bands. No stellar companions were found within detection limits.

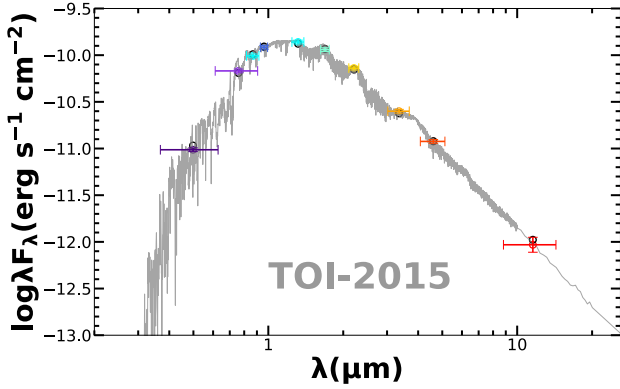


**Fig. 6.** Spectral Energy Distribution (SED) fit of TOI-2015. The gray curve is the best-fitting NextGen atmosphere model, the black circles show the model fluxes, while the colored circles with error bars show the observed fluxes.

We performed a fit using NextGen stellar atmosphere models, with the free parameters being the effective temperature ( $T_{\text{eff}}$ ) and metallicity ([Fe/H]); for the latter we adopted the spectroscopically determined value using MAROON-X data. In addition, we fixed the extinction  $A_V \equiv 0$  due to the proximity of the system to Earth. The resulting fit (Figure 6) has a best-fit  $T_{\text{eff}} = 3200 \pm 75$  K, with a reduced  $\chi^2$  of 1.3. Integrating the model SED gives the bolometric flux at Earth,  $F_{\text{bol}} = 1.552 \pm 0.018 \times 10^{-10}$  erg s $^{-1}$  cm $^{-2}$ , which with the *Gaia* parallax gives the luminosity,  $L_{\text{bol}} = 0.010837 \pm 0.000063$  L $_{\odot}$ . Taking the  $L_{\text{bol}}$  and  $T_{\text{eff}}$  together gives the stellar radius,  $R_{\star} = 0.339 \pm 0.016$  R $_{\odot}$ .

In addition, we derived the stellar mass from the empirical  $M_K$  relations of Mann et al. (2019), giving  $M_{\star} = 0.33 \pm 0.02$  M $_{\odot}$ .

We also checked stellar parameters as obtained from evolutionary modeling using CLES models for low-mass stars (Scuflaire et al. 2008; Fernandes et al. 2019). We used the luminosity derived just above, the metallicity [Fe/H] =  $-0.31 \pm 0.16$  from MAROON-X, and an assumed an age  $>1$  Gyr as inputs. We derived  $M_{\star} = 0.28 \pm 0.06$  M $_{\odot}$ , within 1- $\sigma$  agreement with the stellar mass found above. Other stellar parameters (stellar radius, effective temperature, etc.) are also found to be within 1  $\sigma$  of the values derived above.

### 3.2. Spectroscopic analysis

We determined stellar parameters from the red part of the MAROON-X spectrum (see Figure 7) following the method described in Passegger et al. (2020) using the PHOENIX-ACES model grid (Husser et al. 2013) and assuming a stellar age of 5 Gyr for the evolutionary models (PARSEC, Bressan et al. (2012); Chen et al. (2014, 2015); Tang et al. 2014). With this, we derive parameters of  $T_{\text{eff}} = 3211 \pm 51$  K,  $\log g_{\star} = 5.04 \pm 0.04$ , and [Fe/H] =  $-0.31 \pm 0.16$ . The derived metallicity of [Fe/H] =  $-0.31 \pm 0.16$  is significantly different from the values determined from SpeX and Kast spectra. We note that these spectrographs have lower spectral resolutions, and therefore different determination techniques have been used. As shown by Passegger et al. (2022), who compared different stellar parameter determination techniques, significant differences in the metallicity can be found by different methods, even when used on the same high-resolution spectra.

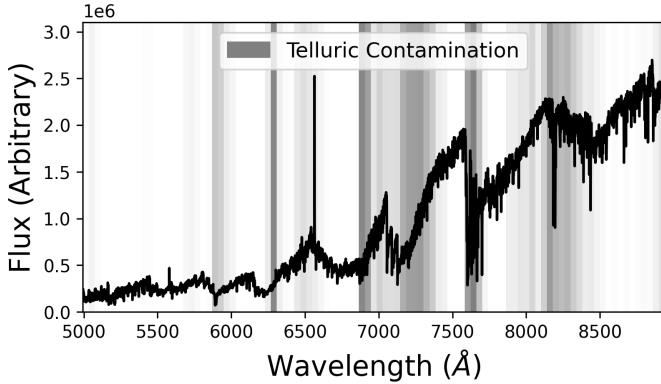


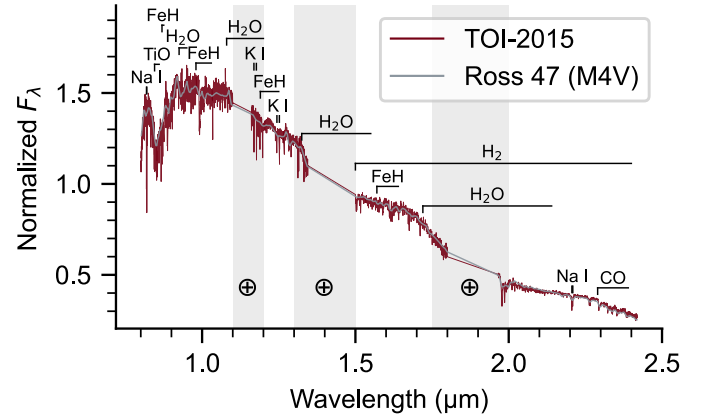
**Fig. 7.** MAROON-X spectrum of TOI-2015. The spectrum of TOI-2015 is shown in black. The gray regions are regions with telluric features in the spectrum, with darker gray indicating more tellurics.

An independent analysis run with the same methods as [Brady et al. \(2024\)](#) recovered similar values for  $T_{\text{eff}}$  ( $3237 \pm 82$  K) and  $[\text{Fe}/\text{H}]$  ( $-0.22 \pm 0.16$ ), which makes sense as both techniques utilize comparisons to PHOENIX model spectra to recover the stellar parameters. However, we note that the [Brady et al. \(2024\)](#) technique tends to perform unreliable for M dwarfs cooler than 3200 K, and the recovered temperature for TOI-2015 falls very close to this limit.

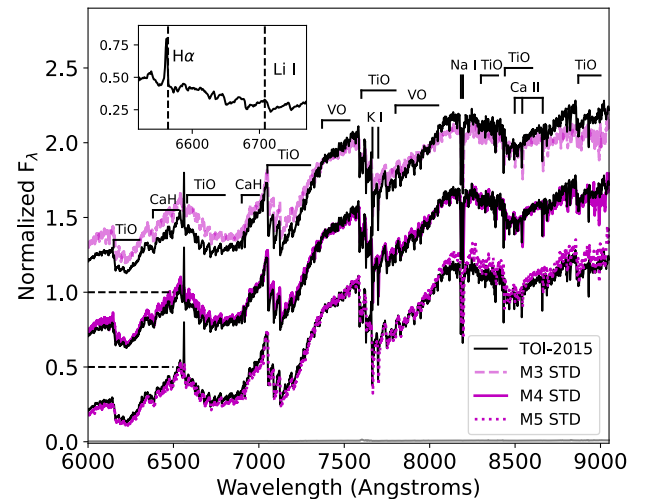
We also followed methods similar to those in [Brady et al. \(2024\)](#) to estimate the stellar  $v \sin i$  by comparing the width of its cross-correlation function with an artificially broadened MAROON-X spectrum of Barnard's Star, which, as an M 4 star ([Kirkpatrick et al. 1991](#)), has a similar spectral type to TOI-2015. Overall, we recovered a  $v \sin i$  value of  $2.1 \pm 0.4$  km s $^{-1}$ . However, we note that, due to MAROON-X's resolution, this method cannot measure  $v \sin i$  values lower than 2 km s $^{-1}$ , meaning that it is possible that TOI-2015 is rotating more slowly than the detection limit of MAROON-X. This value implies that TOI-2015 may be rotating more slowly than the  $v \sin i = 3.2 \pm 0.6$  km s $^{-1}$  quoted in [Jones et al. \(2024\)](#), which was close to the resolution limit of HPF. This discrepancy can be explained by the fact that MAROON-X has a higher resolution than HPF, allowing it to probe longer rotation periods. To be conservative, we thus quote a  $2\sigma$  upper limit of  $v \sin i < 2.9$  km s $^{-1}$  for TOI-2015 from the MAROON-X data. This is in agreement with the 8.7 d photometric rotation period quoted by [Jones et al. \(2024\)](#), which predicts a  $v \sin i \lesssim 2$  km s $^{-1}$ .

Figure 8 shows the SpeX SXD spectrum of TOI-2015. We used the SpeX Prism Library Analysis Toolkit (SPLAT, [Burgasser & Splat Development Team 2017](#)) to compare the spectrum to those of SpeX Prism standards ([Kirkpatrick et al. 2010](#)). We found the best spectral match to be the M4 standard Ross 47 (Gl 213), and we adopted an infrared spectral type of  $M4.0 \pm 0.5$  for TOI-2015. Using SPLAT, we measured the equivalent widths of the  $K$ -band  $\text{Na I}$  and  $\text{Ca I}$  doublets and the  $\text{H}_2\text{O}$ – $\text{K2}$  index ([Rojas-Ayala et al. 2012](#)). Following the [Mann et al. \(2013\)](#) relation between these observables and stellar metallicity, and propagating uncertainties using a Monte Carlo approach (see [Delrez et al. 2022](#)), we estimated an iron abundance of  $[\text{Fe}/\text{H}] = +0.29 \pm 0.13$ .

Figure 9 compares the reduced Shane/Kast red optical spectrum of TOI-2015 to the M3, M4, and M5 dwarf spectral templates from [Bochanski et al. \(2007\)](#). The spectral morphology of TOI-2015 is intermediate between the M4 and M5 templates, suggesting an  $M4.5 \pm 0.5$  optical classification, consistent with the near-infrared type. Both template-based classifications



**Fig. 8.** SpeX SXD spectrum of TOI-2015. The spectrum of TOI-2015 is shown in red, and the SpeX Prism spectrum of the M4 standard Ross 47 is shown in gray for comparison. Strong spectral features of M dwarfs are indicated, and regions of high telluric absorption are shaded.



**Fig. 9.** Normalized Shane/Kast optical spectrum of TOI-2015 (black lines) compared to three SDSS spectral templates from [Bochanski et al. \(2007\)](#), magenta lines). Characteristic spectral features of mid-type M dwarfs are labeled. The inset box shows the 6520–6770 Å region encompassing  $\text{H}\alpha$  (in emission) and  $\text{Li I}$  (not detected).

are also consistent with optical index-based classifications from [Reid et al. \(1995\)](#); [Gizis \(1997\)](#); [Martín et al. \(1999\)](#); [Lépine et al. \(2003\)](#); and [Riddick et al. \(2007\)](#), which span M3.5–M4.5. We detected strong  $\text{H}\alpha$  emission at 6563 Å with an equivalent width of  $-3.09 \pm 0.08$  Å, corresponding to  $\log(L_{\text{H}\alpha}/L_{\text{bol}}) = -4.02 \pm 0.06$  using the  $\chi$  factor relation of [Douglas et al. \(2014\)](#). This strong emission implies an activity age of no more than 5–6 Gyr ([West et al. 2008](#)), while the absence of detectable  $\text{Li I}$  absorption at 6708 Å rules out an age younger than  $\sim 30$  Myr. We measured the metallicity index  $\zeta = 1.057 \pm 0.002$  ([Lépine et al. 2013](#)) which corresponds to a slightly super-solar metallicity of  $[\text{Fe}/\text{H}] = 0.08 \pm 0.20$  using the [Mann et al. \(2013\)](#) calibration. This is formally consistent with the super-solar metallicity inferred from the SpeX data.

### 3.3. Spectral and photometric fitting using Bayesian model averaging

The SpeX SXD spectrum of TOI-2015, alongside photometric data from 2MASS ( $JHK_S$ ), ALLWISE ( $W1, W2$ ), and *Gaia* DR3 ( $G, G_{\text{RP}}$ ), was used for a SED fit using four synthetic spectral

model grids. The SpeX SXD spectrum was convolved to a wavelength resolution of  $R = 200$  to ensure consistent analysis across the different grids. Absolute flux calibration was achieved by scaling the optical part of the SpeX SXD spectrum to match the Gaia XP spectrum (Gaia Collaboration 2023). For the spectral and photometric fitting, we employed four synthetic spectral libraries specifically designed to model the M dwarf regime: BT-Settl CIFIST (Allard et al. 2013), BT-Settl AGSS (Allard et al. 2012), Phoenix ACES (Husser et al. 2013), and SPHINX (Iyer et al. 2023). These libraries offer theoretical spectra and atmospheric models that account for various physical conditions in M dwarfs, making them appropriate for this analysis. The fitting process was carried out using the `species` toolkit (Stolk et al. 2020), which incorporates the nested sampling algorithm from the UltraNest package (Buchner 2023) to efficiently explore parameter space and estimate posterior distributions as well as Bayesian evidence. We adopted empirical relations for the  $T_{\text{eff}}$ , radius, and mass of M dwarfs from Mann et al. (2015) as priors in this analysis, using *Gaia* DR3 magnitudes, parallax, and 2MASS  $K_s$  magnitude as constraints. The model grids cover [Fe/H] from  $-1.0$  to  $+0.5$  dex. A flat prior was used for extinction ( $A_v$ ), with potential values constrained between 0 and 0.2, given the star's proximity. The parameters fit included  $T_{\text{eff}}$ , [Fe/H],  $\log g_{\star}$ , parallax, radius, and extinction. The carbon-to-oxygen (C/O) ratio was also fit for the SPHINX library without any prior. Furthermore, stellar-mass and luminosity estimates were derived from relations involving  $\log g_{\star}$ , radius, parallax, and  $T_{\text{eff}}$ .

We applied a BMA approach to combine the posterior distributions from each synthetic library. This method provides a robust estimation of stellar parameters by accounting for uncertainties between different models, yielding our final estimates for  $T_{\text{eff}}$ , [Fe/H],  $\log g_{\star}$ , parallax, radius, extinction, and, in the case of SPHINX, the C/O ratio. The best-fit synthetic spectrum and the residuals are shown in Figure 10, with the BMA values listed in Table 2. The final values obtained through BMA closely matched the best-fit results from the BT-Settl CIFIST library, since it is the grid with the most evidence. All grids provide a super-solar metallicity for TOI-2015, and the largest discrepancies in the posteriors distributions are found for  $T_{\text{eff}}$  (median values from 3170 K to 3315 K), and therefore, for the stellar radius (median values from  $0.3262$  to  $0.3548 R_{\odot}$ ).

## 4. Planet validation

### 4.1. TESS data validation

The SPOC performed a transit search of Sector 24 on 23 May 2020 (Jenkins 2002; Jenkins et al. 2010, 2020), which yielded a candidate with a 3.35 days period at a signal-to-noise ratio of  $S/N = 13.6$ . The TESS Science Office reviewed the vetting information and issued an alert on 2020 June 19 (Guerrero et al. 2021). The transit signal was also recovered in Sectors 51 and 78, and the transit signature passed all the diagnostic tests presented in the data-validation reports.

The transit depth found was  $9753 \pm 735$  ppm, corresponding to a planet radius of  $3.4 \pm 0.4 R_{\oplus}$  and a period of  $3.34916 \pm 0.00001$  days. A comparison of the odd and even transit depths led to a  $2\sigma$  agreement. The target is quite isolated and no neighboring star was included in the *TESS* aperture (see Figure 1), although TOI-2015 was identified as the likely source of the events.

According to the difference image centroiding test (Twicken et al. 2018) for Sector 24, the host star is located within  $5.058 \pm 2.9$  arcsec of the transit source. This result was then tightened

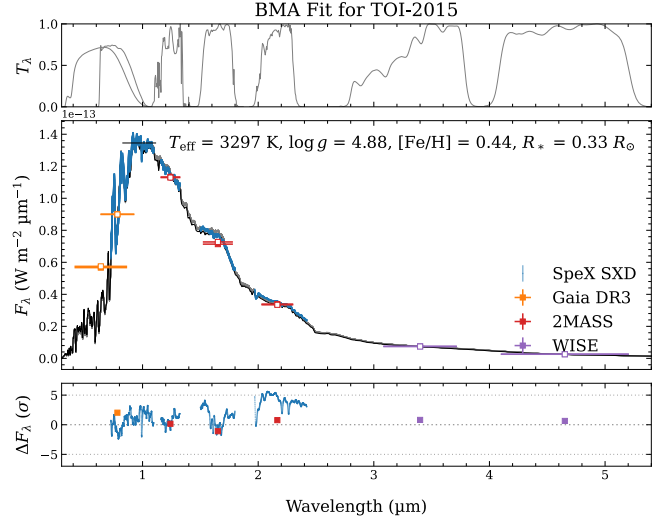


**Fig. 10.** Bayesian Model Averaging (BMA) fit for TOI-2015. The top panel shows the transmission curves of the filters considered, and the bottom panel displays the residuals. The observed SpeX SXD spectrum is shown in blue, while the black line represents the BT-Settl CIFIST synthetic spectrum using the BMA-derived stellar parameters, as shown in Table 1. The fluxes related to the photometry are shown by colors: orange for Gaia DR3, red for 2MASS, and purple for WISE.

up to  $0.806 \pm 3.0$  arcsec in the sector 24–51 search. The transit source location is thus consistent with the host star.

### 4.2. Ground-based photometric follow-up

We used the ground-based photometric observations to *i*) confirm the transit event on the target, *ii*) measure the transit timing variations and *iii*) check for the chromaticity for the transit depth in different wavelengths. Two of the closest neighboring stars to TOI-2015 are TIC 368287010 ( $T_{\text{mag}} = 12.97$ ,  $\Delta T_{\text{mag}} = 0.18$ ) at  $33.3''$  and TIC 368287012 ( $T_{\text{mag}} = 16.49$ ,  $\Delta T_{\text{mag}} = 3.69$ ) at  $37.0''$ . We collected the observations in the  $I + z$ ; Johnson- $I_c$ ; and Sloan- $g'$ ,  $-r'$ ,  $-i'$  and  $z_s$  filters, covering a range from 400 to 1000 nm. This resulted in a non-chromatic dependence in different bands. The measured transit depths are presented in Figure 11.

### 4.3. Archival imaging

We used archival science images of TOI-2015 to exclude the background stellar objects that could be blended with our target in its current position. This kind of object might introduce the same transit event that we observed in our data and skew the physical properties of the system that we obtained from our photodynamical analysis. TOI-2015 has a relatively low proper motion of 64 mas/yr. We used images from POSS-II/DSS (Minkowski & Abell 1963) in 1952 in the  $z$  filter and LCO-HAL-2m0/MuSCAT3 in 2024 in the  $z_s$  filter, and they span 72 years. The target has moved by only  $6.12''$  from 1952 to 2024. There is no stellar background source at the present-day position of TOI-2015 (see Figure 12).

### 4.4. Statistical validation

We used the Tool for Rating Interesting Candidate Exoplanets and Reliability Analysis of Transits Originating from Proximate Stars (TRICERATOPS<sup>8</sup>, Giacalone et al. 2021) package to

<sup>8</sup> TRICERATOPS: <https://github.com/stevengiacalone/triceratops>

**Table 2.** Astrometry, photometry, and spectroscopy stellar properties of TOI-2015.

Star information		
<i>Identifying information</i>		
	TOI 2015	
	TIC 368287008	
	DR3 ID 1270814787767025408	
	2MASS J15283191+2721388	
	WISE J152831.86+272139.5	
Parameter	Value	Source
<i>Parallax and distance</i>		
RA (J2000)	15:28:31.84	(1)
Dec (J2000)	+27:21:39.86	(1)
Parallax (mas)	$21.13 \pm 0.02$	(1)
$\mu_{\text{RA}}$ (mas yr $^{-1}$ )	$-56.244 \pm 0.010$	(1)
$\mu_{\text{Dec}}$ (mas yr $^{-1}$ )	$63.807 \pm 0.014$	(1)
Distance (pc)	$47.32 \pm 0.05$	(1)
<i>Photometric properties</i>		
$TESS_{\text{mag}}$	$12.839 \pm 0.007$	(2)
$V_{\text{mag}}$ (UCAC4)	$16.11 \pm 0.20$	(3)
$B_{\text{mag}}$ (UCAC4)	$17.13 \pm 0.10$	(3)
$J_{\text{mag}}$ (2MASS)	$11.12 \pm 0.02$	(4)
$H_{\text{mag}}$ (2MASS)	$10.52 \pm 0.02$	(4)
$K_{\text{mag}}$ (2MASS)	$10.26 \pm 0.02$	(4)
$G_{\text{mag}}$ (Gaia DR3)	$14.176 \pm 0.001$	(1)
$W1_{\text{mag}}$ (WISE)	$10.098 \pm 0.022$	(5)
$W2_{\text{mag}}$ (WISE)	$9.93 \pm 0.02$	(5)
$W3_{\text{mag}}$ (WISE)	$9.77 \pm 0.04$	(5)
$W4_{\text{mag}}$ (WISE)	9.32	(5)
<i>Spectroscopic and derived parameters</i>		
$T_{\text{eff}}$ (K)	<b><math>3297^{+14}_{-28}</math></b> $3211 \pm 51$ $3200 \pm 75$	(BAM) this work (MAROON-X) this work (SED) this work
$\log g_{\star}$ (dex)	<b><math>5.04 \pm 0.04</math></b> $5.01 \pm 0.02$	[MAROON-X] this work (SED) this work
(Fe/H) (dex)	$+0.29 \pm 0.13$ <b><math>-0.31 \pm 0.16</math></b>	(optical) this work (MAROON-X) this work
$M_{\star}$ [ $M_{\odot}$ ]	$0.33 \pm 0.02$ $0.3043 \pm 0.0067$ <b><math>0.3041^{+0.0353}_{-0.0312}</math></b>	(SED) this work <sup>a</sup> this work (BMA) this work
$R_{\star}$ [ $R_{\odot}$ ]	$0.339 \pm 0.016$ $0.3240 \pm 0.0094$ <b><math>0.3273^{+0.0029}_{-0.0051}</math></b>	(SED) this work <sup>a</sup> this work (BMA) this work
$F_{\text{bol}}$ [erg cm $^{-2}$ s $^{-1}$ ]	$1.552 \pm 0.018 \times 10^{-11}$	(SED) this work
$A_V$ (mag)	$0.02 \pm 0.02$	(SED) this work
$L_{\star}$ ( $L_{\odot}$ )	$0.0322^{+0.0028}_{-0.0025}$	(SED) this work
$\rho_{\star}$ ( $\rho_{\odot}$ )	$8.37^{+1.03}_{-0.98}$	(BMA) this work
Age (Gyr)	$\lesssim 5-6$	(H $\alpha$ ) this work
$v \sin i$ (km s $^{-1}$ )	$\lesssim 2$	(MAROON-X) this work
Spectral type	M4 $\pm 0.5$ M4.5 $\pm 0.5$	(NIR) this work (optical) this work

**Notes.** (1) Gaia EDR3 [Gaia Collaboration \(2021\)](#); (2) *TESS* Input Catalog [Stassun et al. \(2018b\)](#); (3) UCAC4 [Zacharias et al. \(2012\)](#); (4) 2MASS [Skrutskie et al. \(2006\)](#); (5) WISE [Cutri et al. \(2021\)](#). <sup>(a)</sup>Stellar mass and radius values are computed from [Mann et al. \(2015\)](#); [Mann et al. \(2019\)](#). Parameters in bold are the stellar parameters used in priors for photodynamical modeling presented in Section 5.

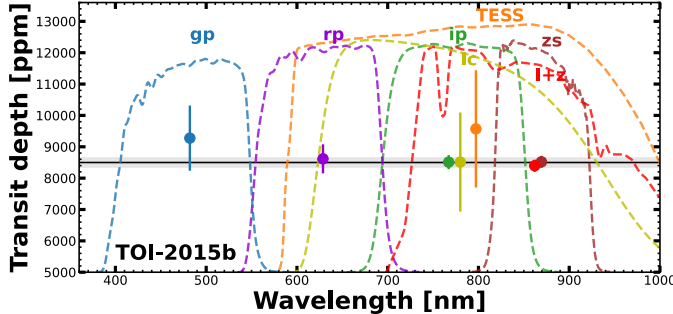


**Fig. 11.** Measured transit depths in different bands (colored dots with error bars) obtained in the global analysis for TOI-2015 b. The horizontal black line corresponds to the depth obtained from the achromatic fit with a  $1\sigma$  error bar (shaded region). All measurements agree with the common transit depth at  $1\sigma$ . Colored dashed lines show the transmission for each filter.

calculate the false positive probability, which allowed us to identify whether a given candidate is a planet or a nearby false positive. TRICERATOPS returns two parameters, which are the false positive probability (FPP) and the nearby false positive probability (NFPP). TRICERATOPS uses the phase-folded *TESS* light curves of the candidate and runs a Bayesian fit of several different possible astrophysical scenarios. It also allows us to implement high-contrast imaging observations in order to improve our results. In our case, we used the 4.1-m SOAR contrast curves described in Section 2.4. Using the *TESS* light curves of TOI-2015 b phase-folded on the orbital periods obtained from the photometric fit (see Section 5). Using ground-based observations (see Section 2.2), the transit event is detected on the target, and thus we excluded other nearby sources, which means that  $\text{NFPP} = 0$  for TOI-2015 b. Typically, *i*) a given candidate is considered statistically validated when  $\text{FPP} < 0.015$  and  $\text{NFPP} < 0.001$ , *ii*) a given candidate is likely a planet if  $\text{FPP} < 0.5$  and  $\text{NFPP} < 0.001$ , and *iii*) a given candidate is a nearby false positive if  $\text{NFPP} > 0.1$ . We ran TRICERATOPS using the TOI-2015 b phase-folded *TESS* light curves and the 4.1-m SOAR high contrast imaging observations. We obtained  $\text{NFPP} = 0$  and  $\text{FPP} = 0.0055 \pm 0.0011$ . TOI-2015 b is a validated planet.

## 5. Global modelling: Photometrics, TTVs, and RVs

We performed a set of photodynamical analyses modeling the *TESS* data, ground-based photometric observations, and the MAROON-X radial velocity measurements jointly using PyTTV (Korth et al. 2023; Korth et al. 2024). The code models the photometry and the radial velocities simultaneously using REBOUND (Rein & Liu 2012; Rein & Spiegel 2015; Tamayo et al. 2020) for dynamical integration and PyTransit (Parviainen 2015; Parviainen & Korth 2020; Parviainen 2020) for transit modeling, and provides posterior densities for the model parameters estimated using Markov chain Monte Carlo (MCMC) sampling in a standard Bayesian parameter estimation framework.

Table G.1 lists the model parameters and their priors. All planetary parameters, except for the  $\log_{10}$  mass and radius ratio, are defined at a reference time of  $t_{\text{ref}} = 2459424.785$  BJD<sub>TDB</sub>. We set uniform priors on the logarithmic masses of the two planets, with ranges designed to aid optimization without constraining the posteriors. For the inner planet's radius ratio, we applied a loosely informative prior based on the visible transit depth, while the outer planet's radius ratio is assigned a dummy

normal prior, as the data cannot constrain it. We set a normal prior on the inner planet's transit center and an uniform prior on the outer planet's mean anomaly (the planets are parameterized differently since one transits and the other does not). A loosely informative prior is set on the inner planet's impact parameter based on the transit fit, and a loosely informative normal prior is used for the outer planet's impact parameter. We did not constrain the outer planet to non-transiting geometries because we are interested in seeing the preferred solutions without informing the analysis that the outer planet does not transit. Additionally, we set zero-centered half-normal priors on the eccentricities,  $\mathcal{N}(0.0, 0.083)$ , allowing for eccentric orbits while biasing against high eccentricities. Finally, we apply a normal prior on the stellar density,  $\mathcal{N}(13, 1.3) \text{ g cm}^{-3}$ , based on stellar characterization.

Since the period of the second planet is unknown, we had to repeat the photodynamical analysis for all plausible period commensurability scenarios that could lead to the observed TTVs. We ignored the scenarios with an inner non-transiting planet and carried out analysis for scenarios where the other planet's orbital period is close to the 2:1, 5:3, 5:2, 4:3 and 3:2 period commensurabilities. For each scenario, we set the prior for the outer planet's period to  $\mathcal{N}(r \times 3.3491408, 0.02)$  days, where  $r$  is the period ratio corresponding to the scenario, and the 3.3491408 days period is derived from the linear ephemeris model.

The analysis starts with a global optimization using the differential evolution method (Storn 1997; Price et al. 2005) implemented in PyTransit (Parviainen 2015). The optimizer starts with a population of parameter vectors drawn from the model prior and clumps the population close to the global posterior mode. After the optimization, we used the clumped parameter vector population to initialize the emcee sampler (Foreman-Mackey et al. 2013), which we then used for MCMC sampling to obtain a sample from the parameter posterior. Finally, we tested the stability of the posterior solution by integrating a subset of posterior samples over 10 000 years.

The best-fit solutions yield differential Bayesian information criterion (BIC – BIC<sub>5:3</sub>) values of 150, 0, –365, 517, and 183 for the 2:1, 5:3, 5:2, 4:3, and 3:2 scenarios, respectively. These results indicate that the BIC favors the 5:2 period commensurability scenario, with the 5:3 scenario emerging as the second-most preferred. However, stability tests reveal that the solutions for the 5:2 and 3:2 scenarios are unstable, leading to the ejection of one of the planets from the system within 10 000 years. Conversely, the solutions for the 2:1, 5:3, and 4:3 scenarios remain stable over the tested period. Among these, the 5:3 scenario is strongly favored over the 2:1 and 4:3 scenarios and also exhibits the smallest orbital inclination differences compared to the other configurations.

Adopting the 5:3 scenario, we find that TOI-2015 b is a sub-Neptune with a radius of  $R_p = 3.309_{-0.011}^{+0.013} R_\oplus$ , a mass of  $M_p = 9.20_{-0.36}^{+0.32} M_\oplus$ , and an eccentricity of  $e_p = 0.0789_{-0.0016}^{+0.0018}$ . The non-transiting planet, TOI-2015 c has a mass of  $M_c = 9.52_{-0.36}^{+0.42} M_\oplus$ , an orbital period of  $P_c = 5.5829$  days, and an eccentricity of  $e_c = 0.0004_{-0.0001}^{+0.0002}$  (see Table 3). Figure 13 shows the TTV data with fits for the 5:3 near-resonance scenario. We also present the results for the 2:1 and 5:2 scenarios in Tables E.1 and F.1.

We also investigated the orbital stability of the 5:2, 5:3, and 2:1 MMR scenarios. To proceed, we extracted 200 configurations from each model posterior, and computed the dynamical evolution of the  $3 \times 200$  configurations over 300 kyr. For these simulations, we used the WHFast integrator (Rein & Tamayo 2015) from the rebound software package (Rein & Liu 2012),

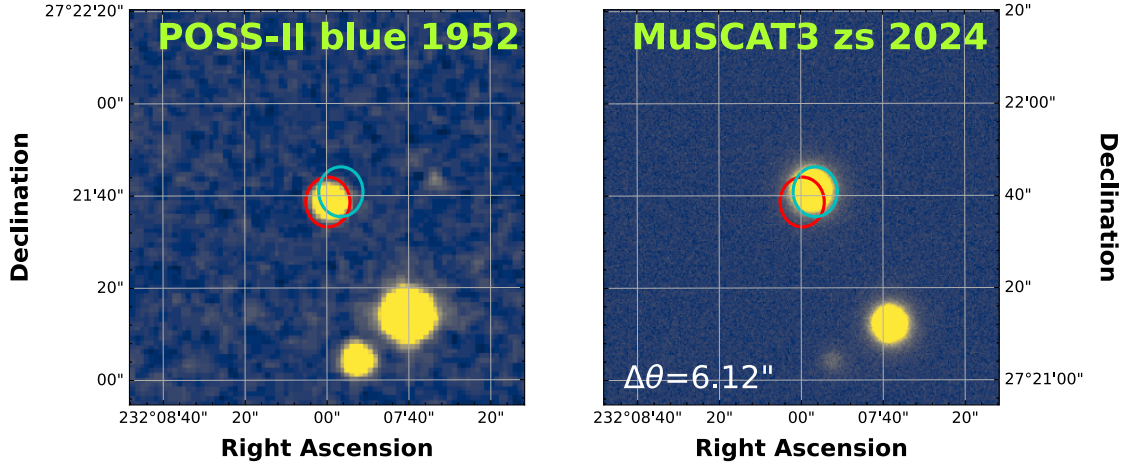


**Fig. 12.** Evolution of TOI-2015 position. The left panel shows an archival image of TOI-2015 taken using a photographic plate on the Palomar Schmidt Telescope in the blue filter. The right panel shows the  $z_s$  image from LCO-HAL-2m0/MuSCAT3 taken in 2024.

**Table 3.** Physical parameters of TOI-2015 system for the 5:3 near-resonance scenario.

Parameter	Unit	TOI-2015 b	TOI-2015 c
Orbital period $P$	days	$3.348237^{+0.000035}_{-0.000030}$	$5.582796^{+0.000042}_{-0.000041}$
Transit-timing $T_0$	BJD <sub>TDB</sub>	$2459424.78570^{+0.00016}_{-0.00015}$	–
Orbital semi-major axis $a$	au	$0.029322 \pm 0.000003$	$0.041232 \pm 0.000004$
Impact parameter $b$	$R_\star$	$0.74346^{+0.0029}_{-0.0030}$	$2.02^{+0.11}_{-0.10}$
Transit duration $W$	hour	$0.9876^{+0.0029}_{-0.0034}$	–
eccentricity $e$	–	$0.0789^{+0.0018}_{-0.0016}$	$0.00033^{+0.0003}_{-0.0002}$
$\sqrt{e} \cos(w)$	–	$0.2624^{+0.0047}_{-0.0042}$	$0.01597^{+0.0060}_{-0.0059}$
$\sqrt{e} \sin(w)$	–	$-0.1008^{+0.0012}_{-0.0082}$	$0.0087^{+0.0023}_{-0.0032}$
Mean anomaly $M$	deg	–	$3.547^{+0.019}_{-0.025}$
Orbital inclination $i$	deg	$87.61 \pm 0.01$	$85.70^{+0.27}_{-0.24}$
Radius ratio $R_p/R_\star$	–	$0.09278^{+0.00035}_{-0.00030}$	–
Scaled semi-major axis $a/R_\star$	–	$19.2811^{+0.0061}_{-0.0060}$	$27.1122 \pm 0.0098$
Planet radius $R_p$	$R_\oplus$	$3.309^{+0.013}_{-0.011}$	–
Planet Mass $M_p$	$M_\oplus$	$9.20^{+0.32}_{-0.35}$	$8.91^{+0.38}_{-0.40}$
Planet density $\rho_p$	g/cm <sup>3</sup>	$1.400^{+0.052}_{-0.056}$	–
Planet irradiation $S_p$	$S_\oplus$	$13.185 \pm 0.387$	$6.68 \pm 0.19$
Equilibrium temperature $T_{\text{eq}}$	K	$530.9^{+2.9}_{-3.9}$	$448 \pm 3$
Planet surface gravity $\log(g_p[\text{cm/s}^2])$	–	$2.915 \pm 0.105$	–
<sup>(a)</sup> TSM	–	$149.4 \pm 5.6$	–
<sup>(a)</sup> ESM	–	$10.8 \pm 0.3$	–

**Notes.** <sup>(a)</sup> TSM and ESM values are computed from Kempton et al. (2018).

with an integration timestep of  $\sim 1/70 P_b$  and a symplectic corrector of the order of 17. The number of system configurations that survived after 300 kyr (no escape, no close encounter) in the 5:2, 5:3, and 2:1 MMR scenarios are 159/200, 200/200, and 172/200, respectively. From these results, the 5:3 MMR scenario contains the largest number of stable configurations. Instead of the small orbital eccentricities, this higher stability rate is largely due to the low mutual inclination of this scenario. Indeed, we also ran simulations on the 5:2 MMR scenario with the hypothesis of co-planarity, and also obtained a higher stability rate. In conclusion, while the 5:3 MMR scenario is more plausible due to the larger number of stable systems, we cannot firmly exclude any of the other scenarios from pure orbital stability considerations.

## 6. Independent analysis of TTV data

An independent analysis of the TTVs of the TOI-2015 b system was conducted using the transit-timing code `NbodyGradient` (Agol et al. 2021b). The fits were initialized near several MMR with period ratios near 4:3, 3:2, 5:3, 2:1 and 5:2. We found that each near-resonance gave fits to the transit times of similar quality, indicating that it is difficult to distinguish between these resonances based solely on transit-timing data, as found by Jones et al. (2024).

However, based on these fits, we find that the eccentricities are much lower in the 5:3 scenario than in the other cases ( $\sim 0.01$  vs  $\sim 0.1$ ). In addition, we find that the masses in the 5:3 solution are very similar to those from our RV fit to the MAROON-X data

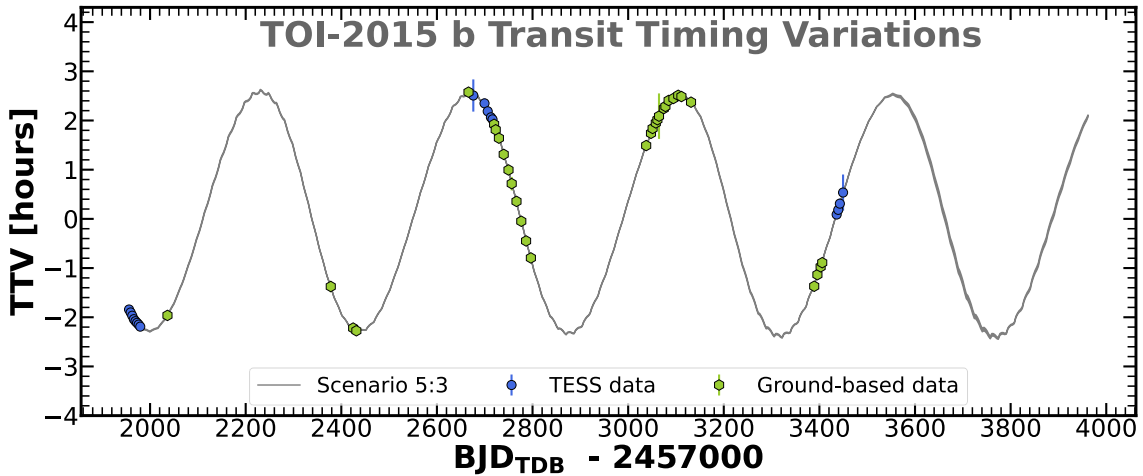


**Fig. 13.** Transit timing variation measurements for TOI-2015 b from *TESS* (blue points) and ground-based (green points) facilities. The gray line is the best-fit transit-timing model for the 5:3 scenario.

with two-planets on circular orbits, indicating that this solution is, in fact, preferred over the others. The eccentricities in this fit are held to zero for convenience, but this turns out to be consistent with the low eccentricity found in the best-fit TTV model near the 5:3 period ratio.

## 7. Planet searches and detection limits from *TESS*

We processed the available 120 s *TESS* data using the SHERLOCK package (Pozuelos et al. 2020; Demory et al. 2020) to recover the original signal corresponding to TOI-2015 b detected by SPOC and search for other potential transiting planets that might remain unnoticed due to detection thresholds. We explored orbital periods from 0.5 to 25 d using ten detrended scenarios corresponding to window sizes ranging from 0.1 to 1.3 d; we refer the reader to Pozuelos et al. (2023) for further details about different searching strategies and to Dévora-Pajares et al. (2024) for a comprehensive update of all of SHERLOCK’s capabilities.

In the first run, we found the signal corresponding to the TOI-2015 b, which allowed us to confirm the detectability of this candidate independently. In the subsequent runs, SHERLOCK did not find any interesting detection, all the signals found being attributable to either intrinsic noise in the light curve not fully decorrelated by our detrending or to spurious detections.

Once we explored the data in the search for extra transiting planets, and since we know that there is at least a second planet in the system, we wanted to establish detection limits with the current data set. To this end we employed the MATRIX package (see, e.g., Dévora-Pajares & Pozuelos 2022; Delrez et al. 2022), which injects synthetic planets into the data using a range of orbital periods, planetary radii, and orbital phases, and tries to recover them, mimicking the procedure conducted by SHERLOCK. The purpose of this analysis is to determine the range of planetary sizes and orbital periods that could be reliably detected in our data set. In particular, we generated 6000 scenarios with the orbital period ranging from 0.5 to 15 d with steps of 0.5 d, and radii from 1 to  $5 R_{\oplus}$  with steps of  $0.2 R_{\oplus}$ . Each radius–period pair was evaluated at ten orbital phases. The results are shown in Figure 14. We found that the planet corresponding to TOI-2015 b falls in a region with a 100% recovery rate. Moreover, we found that any planet larger than  $3.0 R_{\oplus}$  would be easily detectable, with recovery rates higher than 70% at any orbital period explored in this study. In

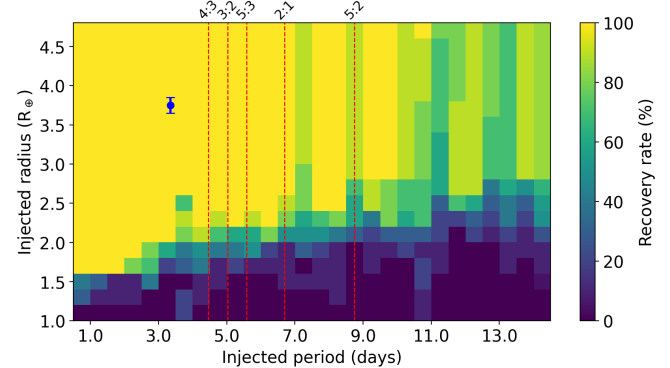


**Fig. 14.** Injection-and-recovery test performed to check the detectability of additional planets in the TOI-2015 system. We explored a total of 6000 different scenarios with the orbital period ranging from 0.5 to 15 days and radius from 1 to  $5 R_{\oplus}$ . Larger recovery rates are presented in green and yellow, while lower recovery rates are shown in blue and darker hues. Planets larger than  $3.0 R_{\oplus}$  with  $P \lesssim 10$  d would be easily detectable. Planets below  $1.5 R_{\oplus}$  would be undetectable, with recovery rates lower than 20% in all cases. The dashed red lines show the MMR possibilities for the non-transiting planet. The blue dot refers to the planet TOI-2015 b.

contrast, planets with radii below  $1.5 R_{\oplus}$  would be undetectable, with recovery rates lower than 20% in all cases. Planets with radii between 1.5 and  $3.0 R_{\oplus}$  represent the transition region with recovery rates from 50 to 100%, with the shorter orbital period being the easier one to detect and vice versa. While the favored solution from the global fit presented in Section 5 corresponds to the MMR 5:3 between planets TOI-2015 b, and c, still other solutions might be possible, such as 4:3, 3:2, 2:1 and 5:2 (see Section 6). We highlight all these possibilities in Figure 14, and we conclude that in all the cases, any transiting planet larger than  $2.0 R_{\oplus}$  should be easily detectable, while smaller transiting planets might remain undetected in the current data set, and hence we cannot entirely rule out the transiting nature of planet c.

## 8. Discussion

### 8.1. Mass-radius and composition

Analyzing the observations from the *TESS* mission together with ground-based photometry and RV measurements collected with

the MAROON-X spectrograph, we confirm the planetary nature of the transiting planet TOI-2015 b around its M4-dwarf host star. We find that the transiting planet TOI-2015 b has a radius and mass of  $R_p = 3.309^{+0.013}_{-0.011} R_\oplus$  and  $M_p = 9.20^{+0.32}_{-0.36} M_\oplus$ , respectively. This results in a mean density of  $\rho_p = 1.400^{+0.052}_{-0.056} \text{ g cm}^{-3}$ , which is indicative of a Neptune-like composition. We present a comparative analysis of the mass and radius of TOI-2015 b with other transiting exoplanets, and composition models from Aguichine et al. (2021) and Lopez & Fortney (2014). The models of Aguichine et al. (2021) considered the mass-radius relation inferred from the water-rich composition models. These models assume a  $\text{H}_2\text{O}$ -dominated atmosphere on top of a high-pressure water layer. We computed the mass-radius relationship from Aguichine et al. (2021) for different water fractions, and for a planetary equilibrium temperature of  $T_{\text{eq}} = 500\text{K}$  (i.e. the equilibrium temperature closest to the one for TOI-2015 b). We assumed a core-mass fraction of  $x_{\text{core}} = 0.3$  (i.e., Earth-like interior composition):

$$\log_{10}(R_p) = a \log_{10}(M_p) + \exp[-d \times (\log_{10}(M_p) + c)] + b, \quad (1)$$

where  $R_p$  is the planet radius in  $R_\oplus$ ,  $M_p$  is the planet mass in  $M_\oplus$ , and  $a$ ,  $b$ ,  $c$ , and  $d$  are coefficients obtained by the Aguichine et al. (2021) fits. The results are shown in Figure 15 (solid colored lines). Based on this preliminary comparison, TOI-2015 b is compatible with a high water-mass fraction of 70%.

We also performed a similar analysis assuming a composition based on a rocky core surrounded by a hydrogen and helium envelope (Lopez & Fortney 2014). These models are generated for planets with masses from 1 to  $20 M_\oplus$ , ages from 100 Myr to 10 Gyr, incident flux from 0.1 to  $1000 F_\oplus$ , and envelope fractions from 0.01 to 20%. We used the tabulated mass-radius relations from the interior models of Lopez & Fortney (2014) for different hydrogen-helium ( $\text{H}_2/\text{He}$ ) fractions, assuming a planet incident flux of  $S_p = 10 S_\oplus$  (i.e., incident flux closest to the one for TOI-2015 b) and systems older than 1 Gyr. Figure 15 shows the mass-radius models (dashed colored lines). In this case, we find that the properties of TOI-2015 b are consistent with a gaseous envelope with a mass fraction of  $f_{\text{env}} \approx 10\%$  of the mass of the planet.

Our results show that models with water-rich and hydrogen-helium envelopes provide equally good matches to the planet density. A future measurement of the transmission spectrum of TOI-2015 b with the *JWST* might help break this degeneracy by providing a direct atmospheric composition of the upper layers of the outer envelope of the planet's atmosphere.

## 8.2. Location in the period–radius diagram

Based on our photodynamical analysis of the system, TOI-2015 b has a period of  $P_b = 3.35$  days. In Figure 16, we plotted the planet radius as a function of the orbital period of transiting exoplanets, along with the boundaries of the Neptune-desert. TOI-2015 b is located within a region between the “Neptune-desert” and “savanna”, defined as the “Neptunian-ridge” by Castro-González et al. (2024). This work suggests that the evolutionary mechanisms that bring planets to the Neptunian ridge might be similar to those that bring larger exoplanets to the hot-Jupiter ( $\approx 3\text{--}5$  days) region. TOI-2015 b has a low eccentricity of  $e_b = 0.0770^{+0.0016}_{-0.0018}$ . This eccentricity is not high enough to start the HEM (high-eccentricity migration) (Fortney et al. 2021; Bourrier et al. 2023).

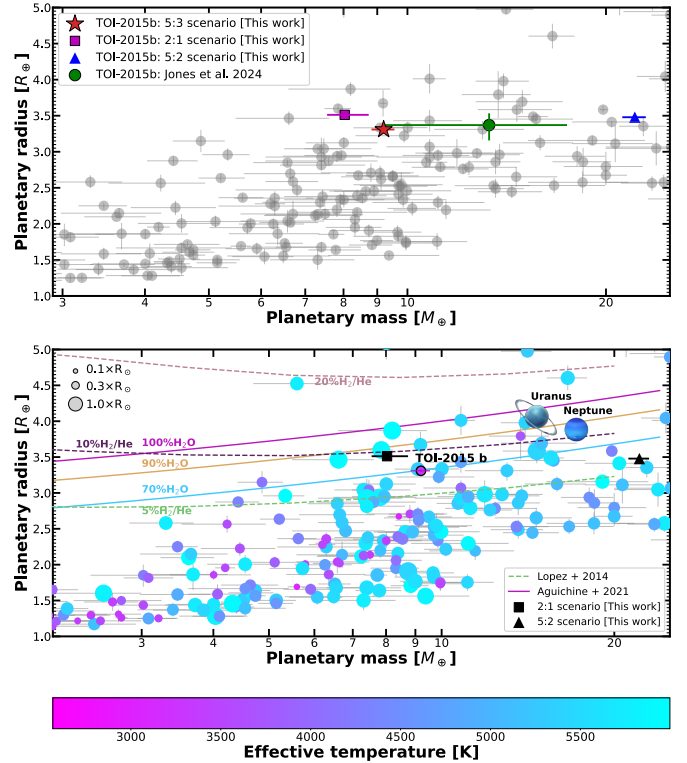


**Fig. 15.** Planetary radius as function of planetary mass of known transiting exoplanets well characterized, with radius and mass precisions better than 10% and 20%, respectively. Data are extracted from TEPCat (Southworth 2011). Top panel shows the comparison between the planetary parameters for TOI-2015 b. The red star shows our updated measurements, while the green dot with error bars shows the planetary parameters derived by Jones et al. (2024). We also highlighted the planetary parameters for other scenarios 2:1 (magenta square) and 5:2 (blue triangle). Bottom panel shows the comparison between TOI-2015 b to other transiting planetary systems. The systems are colored according to the stellar effective temperature. The size of the points is scaled according to the stellar radius. Dashed lines show the mass-radius composition models from Lopez & Fortney (2014). We display mass-radius curves for hydrogen-helium compositions of 5%, 10% and 20%  $\text{H}_2/\text{He}$ . We assumed a planet with an incident flux of  $S_p = 10 S_\oplus$ , and an age of  $> 1$  Gyr. The solid lines present the mass-radius composition models from Aguichine et al. (2021). We display mass-radius curves for water-rich compositions of 70%, 90% and 100%  $\text{H}_2\text{O}$ . We assumed a planetary equilibrium temperature of  $T_{\text{eq}} = 500\text{K}$  and a core mass fraction of  $x_{\text{core}} = 0.3$ . We also highlighted the planetary parameters for other scenarios 2:1 (black square) and 5:2 (black triangle). Two Solar System planets (Uranus and Neptune) are also displayed.

To account for the large-amplitude transit timing variations of TOI-2015 b, we identified an outer non-transiting companion likely to be in a 5:3 near-resonance motion, TOI-2015 c. Our TTV fit (Figure 13) implies an orbital period of  $P_c = 5.582904^{+0.000044}_{-0.000043}$  days, a mass of  $M_c = 8.91^{+0.38}_{-0.40} M_\oplus$ , and an eccentricity of  $e_c = 0.00033^{+0.0003}_{-0.0002}$ . The presence of this companion in the system might be partly responsible for inward migration of TOI-2015 b. The location of TOI-2015 b in the radius-period diagram (Figure 16), the presence of the companion, and future spin-orbit angle measurements will provide us with some more insights into the formation and evolution history of the system.

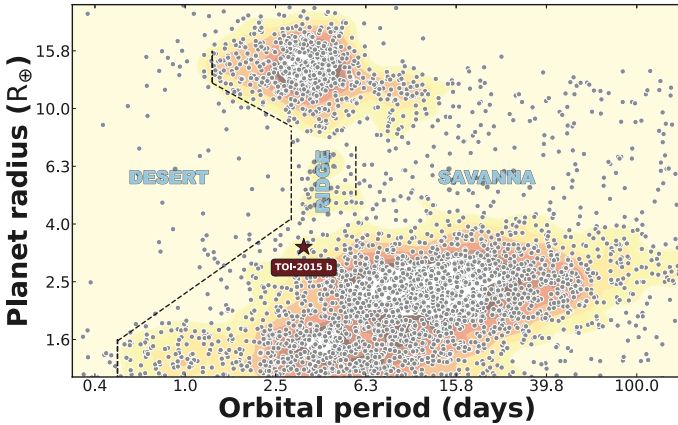


**Fig. 16.** Planetary radius versus orbital period diagram of known transiting exoplanets. Data are extracted from NASA Archive of Exoplanets. The location of the Neptunian desert, ridge, and savanna derived by Castro-González et al. (2024) are highlighted. TOI-2015 b is well placed in the Neptunian-ridge region. This plot is made using nep-des (<https://github.com/castro-gzlx/nep-des>).

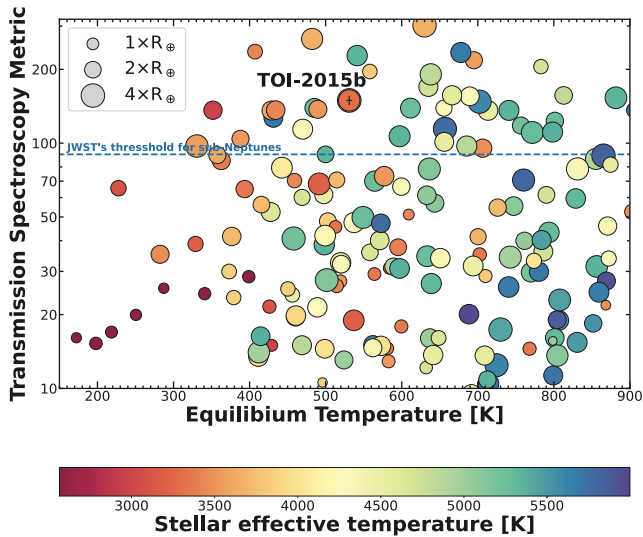


**Fig. 17.** Feasibility of TOI-2015 b for transmission spectroscopy studies. The transmission spectroscopy metric (TSM; Kempton et al. (2018)) as a function of the planetary equilibrium temperature of all known transiting exoplanets with mass measurement is shown. Data are extracted from the NASA Exoplanets Archive. The size of the points scales according to the planetary radius. The points are colored according to the stellar effective temperature. TOI-2015 b is highlighted by the black circle and error bars.

### 8.3. Potential for atmospheric characterization for TOI-2015 b

To quantify the suitability of transiting exoplanets for atmospheric characterization through transmission spectroscopy, we used the transmission spectroscopy metric (TSM) derived by Kempton et al. (2018). By combining the planetary radius, mass, equilibrium temperature, and the infrared stellar brightness, we find that TOI-2015 b has a TSM of  $149.4 \pm 5.6$ . Figure 17 plots the TSM as a function of the planetary equilibrium temperature for transiting exoplanets with mass measurements. This shows that TOI-2015 b is one of the best sub-Neptune planets for atmospheric exploration with the *JWST*.

We further explored the potential of TOI-2015 b for transmission spectroscopy with the *JWST* through spectral simulations

for a suite of atmospheric scenarios. We adopted TauREX 3 (Al-Refaie et al. 2021) to simulate the synthetic transmission spectra. TOI-2015 b could retain an H/He-dominated and water-rich atmosphere (Sect 8.1). We modeled H/He atmospheres with 1× and 100× scaled solar abundances using the atmospheric chemical equilibrium module of Agúndez et al. (2012), including collision-induced absorption by H<sub>2</sub>-H<sub>2</sub> and H<sub>2</sub>-He (Abel et al. 2011, 2012; Fletcher et al. 2018). For each chemical setup, we considered the cases of clear and hazy atmospheres. The haze was modeled using Mie scattering with the formalism of Lee et al. (2013), assuming the same haze parameters as in previous studies (Orell-Miquel et al. 2023; Goffo et al. 2024). We note that a super-solar metallicity is typically expected for sub-Neptune-sized planets (e.g., Fortney et al. 2013; Thorngren et al. 2016), while the planetary equilibrium temperature ( $T_{\text{eq}}$ ) within  $T_{\text{eq}} \approx 400$ –600 K also points to a high degree of haziness due to inefficient haze removal (Gao & Zhang 2020; Ohno & Tanaka 2021; Yu et al. 2021). Moreover, we modeled the case of a pure H<sub>2</sub>O atmosphere.

The ExoTETHyS (Morello et al. 2021) package has been used to simulate the corresponding *JWST* spectra with the NIRISS-SOSS ( $\lambda = [0.6 \mu\text{m}$ – $2.8 \mu\text{m}$ ]), NIRSpec-G395H ( $\lambda = [2.88 \mu\text{m}$ – $5.20 \mu\text{m}$ ]), and MIRI-LRS ( $\lambda = [5 \mu\text{m}$ – $12 \mu\text{m}$ ]) instrumental modes. The ExoTETHyS code has been cross-validated against the Exoplanet Characterization Toolkit (ExoCTK, Bourque et al. 2021) and PandExo (Batalha et al. 2017) in a series of previous studies (Murgas et al. 2021; Espinoza et al. 2022; Luque et al. 2022a,b; Chaturvedi et al. 2022; Lillo-Box et al. 2023; Orell-Miquel et al. 2023; Palle et al. 2023; Goffo et al. 2024). We conservatively increased the uncertainty estimates by 20%. We considered wavelength bins with a spectral resolution of  $R \sim 100$  for NIRISS and NIRSpec, and a constant bin size of  $0.25 \mu\text{m}$  for MIRI-LRS observations, following the recommendations from recent *JWST* Early Release Science papers (Carter et al. 2024; Powell et al. 2024).

Figure 18 shows the synthetic transmission spectra for the atmospheric configurations described above. The H/He model atmospheres exhibit strong H<sub>2</sub>O and CH<sub>4</sub> absorption features of  $\geq 100$ –1000 ppm (parts per million), depending on metallicity and haze, while the steam H<sub>2</sub>O atmosphere has absorption features  $\leq 100$  ppm. The predicted error bars for a single transit observation are 60–273 ppm (mean error 110 ppm) for NIRISS-SOSS, 86–256 ppm (mean error 123 ppm) for NIRSpec-G395H, and 125–190 ppm (mean error 144 ppm) for MIRI-LRS. Based on our simulations, a single transit observation with NIRSpec-G395H or NIRISS-SOSS is well suited to detecting an H/He atmosphere, while at least four transit observations may be required to reveal features in the case of a steam atmosphere.

## 9. Conclusion

In this paper, we present a photodynamical analysis of the TOI-2015 exoplanetary system including the *TESS* and ground-based photometry, together with RV measurements obtained with the MAROON-X spectrograph (Section 2.3.1). To account for large-amplitude TTVs, the gravitational interaction between the planets is also included in our analysis. The host star is well characterized using optical and near-infrared spectroscopic observations obtained by MAROON-X, Shane/KAST, and Magellan/FIRE spectrographs, together with SED (section 3.1), BMA (section 3.3), and stellar evolutionary models. The target was observed by the *TESS* mission in Sectors 24, 51, and 78 with a 2-min cadence. The

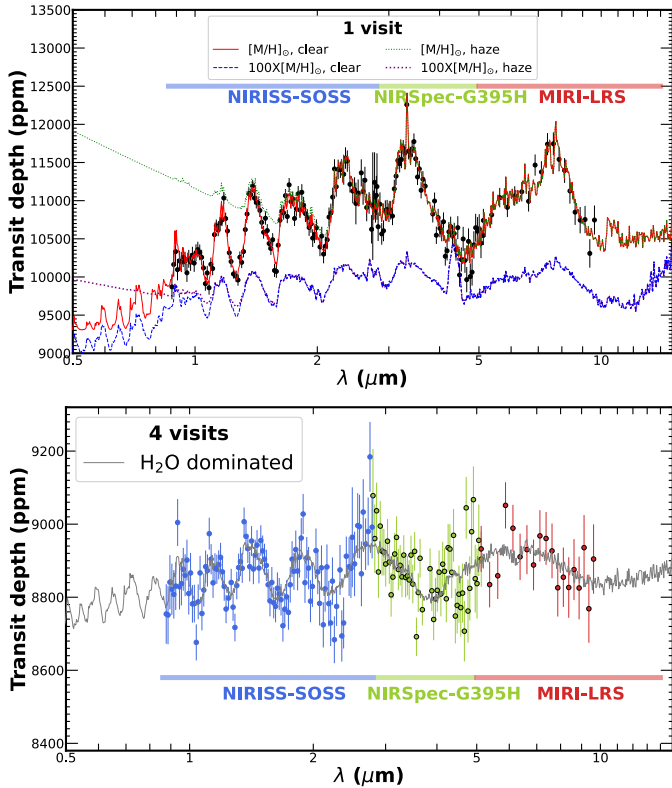


**Fig. 18.** Simulated synthetic atmospheric transmission spectra of TOI-2015 b. Top: fiducial models for clear or hazy H/He atmospheres with scaled solar abundances. Bottom: model for steam H<sub>2</sub>O atmosphere. Simulated measurements with error bars are shown for the observation of one (top) or four (bottom) transits with *JWST* NIRISS-SOSS, NIRSpec-G395H, and MIRI-LRS configurations.

intensive ground-based photometric observations were collected using SPECULOOS-North/Artemis-1m0, SAINT-EX-1m0, MuSCAT, MuSCAT2, LCOGT-2m0/MuSCAT3, LCOGT-1m0, TRAPPIST-North/-South-0.6m, TUBITAK-1m0, IAC80, OSN-1.5m and CAHA-1.23m telescopes (Section 2.2). The photodynamical analysis was performed using the PyTTV pipeline developed by Korth et al. (2023); Korth et al. (2024) (Section 5), and an independent analysis (Section 6) was performed using the NbodyGradient code (Agol et al. 2021b). TOI-2015 is a  $K = 10.3$  mag M4-type dwarf with a subsolar metallicity of  $[Fe/H] = -0.31 \pm 0.16$ , an effective temperature of  $T_{\text{eff}} = 3211 \pm 51$  K, and a surface gravity of  $\log g_{\star} = 5.04 \pm 0.04$  (cgs).

The TOI-2015 system is composed of two sub-Neptune exoplanets. The inner planet, TOI-2015 b is a transiting sub-Neptune at  $P_b = 3.35$  days, with a radius of  $R_p = 3.31 \pm 0.01 R_{\oplus}$  and a mass of  $M_p = 9.86 \pm 0.37 M_{\oplus}$ . To place TOI-2015 b in context within the exoplanet population, we plot the radius-mass diagram (Figure 15) for transit exoplanets with mass measurements. As a preliminary comparison, the planet has a degeneracy in its interior composition based on the mass-radius composition models from Lopez & Fortney (2014) and Aguichine et al. (2021). The measurement of a transmission spectrum from the *JWST* can help to break this degeneracy by providing the planet's atmospheric composition.

The transit events of TOI-2015 b exhibit large TTVs indicative of an outer companion in the system, TOI-2015 c. Our best-fit solution places the planet near a 5:3 resonance with an orbital period of  $P_c = 5.58$  days, a mass of  $M_p = 9.20^{+0.32}_{-0.35} M_{\oplus}$ ,

and an eccentricity of  $e_b = 0.0789^{+0.0018}_{-0.0016}$ . Other scenarios for TOI-2015 c might be possible, such as the 2:1, 5:2, 3:2 and 4:3 resonances. More photometric data and RV measurements are required in order to break this degeneracy on the orbital period of TOI-2015 c.

## Data availability

The *TESS* photometric observations that we used in this work are available via the Mikulski Archive for Space Telescopes (MAST) and the ExoFOP-*TESS* platform. All ground-based photometric observations are also available via the ExoFOP-*TESS* platform. RV measurements collected with the MAROON-X spectrograph are available in Table 1.

## References

Abel, M., Frommhold, L., Li, X., & Hunt, K. L. C. 2011, *J. Phys. Chem. A*, **115**, 6805  
 Abel, M., Frommhold, L., Li, X., & Hunt, K. L. C. 2012, *J. Chem. Phys.*, **136**, 044319  
 Agol, E., Steffen, J., Sari, R., & Clarkson, W. 2005, *MNRAS*, **359**, 567  
 Agol, E., Dorn, C., Grimm, S. L., et al. 2021a, *Planet. Sci. J.*, **2**, 1  
 Agol, E., Hernandez, D. M., & Langford, Z. 2021b, *MNRAS*, **507**, 1582  
 Aguichine, A., Mousis, O., Deleuil, M., & Marcq, E. 2021, *ApJ*, **914**, 84  
 Agúndez, M., Venot, O., Iro, N., et al. 2012, *A&A*, **548**, A73  
 Al-Refaie, A. F., Cheangat, Q., Waldmann, I. P., & Tinetti, G. 2021, *ApJ*, **917**, 37  
 Allard, F., Homeier, D., & Freytag, B. 2012, *Philos. Trans. Roy. Soc. Lond. Ser. A*, **370**, 2765  
 Allard, F., Homeier, D., Freytag, B., Schaffenberger, W., & Rajpurohit, A. S. 2013, *Mem. Soc. Astron. Ital. Suppl.*, **24**, 128  
 Aller, A., Lillo-Box, J., Jones, D., Miranda, L. F., & Barceló Forteza, S. 2020, *A&A*, **635**, A128  
 Barkaoui, K., Burdanov, A., Hellier, C., et al. 2019, *AJ*, **157**, 43  
 Batalha, N. E., Mandell, A., Pontoppidan, K., et al. 2017, *PASP*, **129**, 064501  
 Baştürk, Ö., Hinse, T. C., Özavci, et al. 2015, *ASP Conf. Ser.*, **496**, 370  
 Bean, J. L., Seifahrt, A., Hartman, H., et al. 2010, *ApJ*, **713**, 410  
 Bochanski, J. J., West, A. A., Hawley, S. L., & Covey, K. R. 2007, *AJ*, **133**, 531  
 Bourque, M., Espinoza, N., Filippazzo, J., et al. 2021, <https://doi.org/10.5281/zenodo.4556063>  
 Bourrier, V., Attia, O., Mallonn, M., et al. 2023, *A&A*, **669**, A63  
 Brady, M., Bean, J. L., Seifahrt, A., et al. 2024, *AJ*, **168**, 67  
 Bressan, A., Marigo, P., Girardi, L., et al. 2012, *MNRAS*, **427**, 127  
 Brown, T. M., Baliber, N., Bianco, F. B., et al. 2013, *PASP*, **125**, 1031  
 Buchner, J. 2023, *Statist. Surv.*, **17**, 169  
 Burdanov, A. Y., de Wit, J., Gillon, M., et al. 2022, *PASP*, **134**, 105001  
 Burgasser, A. J., & Splat Development Team 2017, *ASI Conf. Ser.*, **14**, 7  
 Carter, A. L., May, E. M., Espinoza, N., et al. 2024, *Nat. Astron.*, **8**, 1008  
 Castro-González, A., Bourrier, V., Lillo-Box, J., et al. 2024, *A&A*, **689**, A250  
 Chaturvedi, P., Bluhm, P., Nagel, E., et al. 2022, *A&A*, **666**, A155  
 Chen, Y., Girardi, L., Bressan, A., et al. 2014, *MNRAS*, **444**, 2525  
 Chen, Y., Bressan, A., Girardi, L., et al. 2015, *MNRAS*, **452**, 1068  
 Collins, K. A., Kielkopf, J. F., Stassun, K. G., & Hessman, F. V. 2017, *AJ*, **153**, 77  
 Cushing, M. C., Vacca, W. D., & Rayner, J. T. 2004, *PASP*, **116**, 362  
 Cutri, R. M., Wright, E. L., Conrow, T., et al. 2021, *VizieR Online Data Catalog*, II/328  
 Deck, K. M., & Agol, E. 2016, *ApJ*, **821**, 96  
 Delrez, L., Gillon, M., Queloz, D., et al. 2018, arXiv e-prints [arXiv:1806.11205]  
 Delrez, L., Murray, C. A., Pozuelos, F. J., et al. 2022, *A&A*, **667**, A59  
 Demory, B. O., Pozuelos, F. J., Gómez Maqueo Chew, Y., et al. 2020, *A&A*, **642**, A49  
 Dévora-Pajares, M., & Pozuelos, F. J. 2022, <https://doi.org/10.5281/zenodo.6570832>  
 Dévora-Pajares, M., Pozuelos, F. J., Thuillier, A., et al. 2024, *MNRAS*, **532**, 4752  
 Dorn, C., Venturini, J., Khan, A., et al. 2017, *A&A*, **597**, A37  
 Douglas, S. T., Agüeros, M. A., Covey, K. R., et al. 2014, *ApJ*, **795**, 161  
 Espinoza, N., Pallé, E., Kemmer, J., et al. 2022, *AJ*, **163**, 133  
 Fernandes, C. S., Grootel, V. V., Salmon, S. J. A. J., et al. 2019, *ApJ*, **879**, 94  
 Fletcher, L. N., Gustafsson, M., & Orton, G. S. 2018, *ApJS*, **235**, 24  
 Foreman-Mackey, D., Hogg, D. W., Lang, D., & Goodman, J. 2013, *PASP*, **125**, 306  
 Fortney, J. J., Mordasini, C., Nettelmann, N., et al. 2013, *ApJ*, **775**, 80

Fortney, J. J., Dawson, R. I., & Komacek, T. D. 2021, *J. Geophys. Res. (Planets)*, **126**, e06629

Fukui, A., Narita, N., Tristram, P. J., et al. 2011, *PASJ*, **63**, 287

Gaia Collaboration (Brown, A. G. A., et al.) 2021, *A&A*, **650**, C3

Gaia Collaboration (Vallenari, A., et al.) 2023, *A&A*, **674**, A1

Gao, P., & Zhang, X. 2020, *ApJ*, **890**, 93

Garcia, L. J., Timmermans, M., Pozuelos, F. J., et al. 2022, *MNRAS*, **509**, 4817

Gavel, D., Kupke, R., Dillon, D., et al. 2014, *SPIE Conf. Ser.*, **9148**, 914805

Giacalone, S., Dressing, C. D., Jensen, E. L. N., et al. 2021, *AJ*, **161**, 24

Gillon, M., Jehin, E., Magain, P., et al. 2011, *EPJ Web Conf.*, **11**, 06002

Gillon, M., Jehin, E., Lederer, S. M., et al. 2016, *Nature*, **533**, 221

Gillon, M., Triaud, A. H. M. J., Demory, B.-O., et al. 2017, *Nature*, **542**, 456

Gizis, J. E. 1997, *AJ*, **113**, 806

Goffo, E., Chaturvedi, P., Murgas, F., et al. 2024, *A&A*, **685**, A147

Guerrero, N. M., Seager, S., Huang, C. X., et al. 2021, *ApJS*, **254**, 39

Hamuy, M., Walker, A. R., Suntzeff, N. B., et al. 1992, *PASP*, **104**, 533

Hamuy, M., Suntzeff, N. B., Heathcote, S. R., et al. 1994, *PASP*, **106**, 566

Henry, T. J. 1994, *Am. Astron. Soc. Meeting Abstracts*, **184**, 51.04

Henry, T. J., Jao, W.-C., Subasavage, J. P., et al. 2006, *AJ*, **132**, 2360

Holman, M. J., & Murray, N. W. 2005, *Science*, **307**, 1288

Husser, T. O., Wende-von Berg, S., Dreizler, S., et al. 2013, *A&A*, **553**, A6

Iyer, A. R., Line, M. R., Muirhead, P. S., Fortney, J. J., & Gharib-Nezhad, E. 2023, *ApJ*, **944**, 41

Jehin, E., Gillon, M., Queloz, D., et al. 2011, *The Messenger*, **145**, 2

Jehin, E., Gillon, M., Queloz, D., et al. 2018, *The Messenger*, **174**, 2

Jenkins, J. M. 2002, *ApJ*, **575**, 493

Jensen, E. 2013, Astrophysics Source Code Library [[record ascl:1306.007](#)]

Jenkins, J. M., Chandrasekaran, H., McCauliff, S. D., et al. 2010, *SPIE Conf. Ser.*, **7740**, 77400D

Jenkins, J. M., Twicken, J. D., McCauliff, S., et al. 2016, *SPIE Conf. Ser.*, **9913**, 99133E

Jenkins, J. M., Tenenbaum, P., Seader, S., et al. 2020, *Kepler Data Processing Handbook: Transiting Planet Search*, Kepler Science Document KSCI-19081-003

Jones, S. E., Stefánsson, G., Masuda, K., et al. 2024, *AJ*, **168**, 93

Kempton, E. M. R., Bean, J. L., Louie, D. R., et al. 2018, *PASP*, **130**, 114401

Kipping, D. M. 2013, *MNRAS*, **435**, 2152

Kirkpatrick, J. D., Henry, T. J., & McCarthy, Donald W. J. 1991, *ApJS*, **77**, 417

Kirkpatrick, J. D., Looper, D. L., Burgasser, A. J., et al. 2010, *ApJS*, **190**, 100

Korth, J., Gandolfi, D., Šubjak, J., et al. 2023, *A&A*, **675**, A115

Korth, J., Chaturvedi, P., Parviainen, H., et al. 2024, *ApJ*, **971**, L28

Kupke, R., Gavel, D., Roskosi, C., et al. 2012, *SPIE Conf. Ser.*, **8447**, 84473G

Lee, J.-M., Heng, K., & Irwin, P. G. J. 2013, *ApJ*, **778**, 97

Lépine, S., Rich, R. M., & Shara, M. M. 2003, *AJ*, **125**, 1598

Lépine, S., Hilton, E. J., Mann, A. W., et al. 2013, *AJ*, **145**, 102

Lillo-Box, J., Gandolfi, D., Armstrong, D. J., et al. 2023, *A&A*, **669**, A109

Lopez, E. D., & Fortney, J. J. 2014, *ApJ*, **792**, 1

Luque, R., Fulton, B. J., Kumimoto, M., et al. 2022a, *A&A*, **664**, A199

Luque, R., Nowak, G., Hirano, T., et al. 2022b, *A&A*, **666**, A154

Mancini, L., Southworth, J., Ciceri, S., et al. 2013, *A&A*, **551**, A11

Mancini, L., Southworth, J., Raia, G., et al. 2017, *MNRAS*, **465**, 843

Mann, A. W., Brewer, J. M., Gaidos, E., Lépine, S., & Hilton, E. J. 2013, *AJ*, **145**, 52

Mann, A. W., Feiden, G. A., Gaidos, E., Boyajian, T., & von Braun, K. 2015, *ApJ*, **804**, 64

Mann, A. W., Dupuy, T., Kraus, A. L., et al. 2019, *ApJ*, **871**, 63

Martín, E. L., Delfosse, X., Basri, G., et al. 1999, *AJ*, **118**, 2466

McCully, C., Volgenau, N. H., Harbeck, D.-R., et al. 2018, *SPIE Conf. Ser.*, **10707**, 107070K

McGurk, R., Rockosi, C., Gavel, D., et al. 2014, *SPIE Conf. Ser.*, **9148**, 91483A

Miller, J. S., & Stone, R. P. S. 1994, *The Kast Double Spectrograph*, Tech. Rep. 66, University of California Lick Observatory Technical Reports

Minkowski, R. L., & Abell, G. O. 1963, in *Basic Astronomical Data: Stars and Stellar Systems*, ed. K. A. Strand, 481

Morello, G., Zingales, T., Martin-Lagarde, M., Gastaud, R., & Lagage, P.-O. 2021, *AJ*, **161**, 174

Murgas, F., Astudillo-Defru, N., Bonfils, X., et al. 2021, *A&A*, **653**, A60

Narita, N., Fukui, A., Kusakabe, N., et al. 2015, *J. Astron. Telesc. Instrum. Syst.*, **1**, 045001

Narita, N., Fukui, A., Kusakabe, N., et al. 2019, *J. Astron. Telesc. Instrum. Syst.*, **5**, 015001

Narita, N., Fukui, A., Yamamoto, T., et al. 2020, *SPIE Conf. Ser.*, **11447**, 114475K

Ohno, K., & Tanaka, Y. A. 2021, *ApJ*, **920**, 124

Orell-Miquel, J., Nowak, G., Murgas, F., et al. 2023, *A&A*, **669**, A40

Palle, E., Orell-Miquel, J., Brady, M., et al. 2023, *A&A*, **678**, A80

Parviainen, H. 2015, *MNRAS*, **450**, 3233

Parviainen, H. 2020, *MNRAS*, **499**, 1633

Parviainen, H., & Korth, J. 2020, *MNRAS*, **499**, 3356

Parviainen, H., Palle, E., Zapatero-Osorio, M. R., et al. 2020, *A&A*, **633**, A28

Passegger, V. M., Bello-García, A., Ordieres-Meré, J., et al. 2020, *A&A*, **642**, A22

Passegger, V. M., Bello-García, A., Ordieres-Meré, J., et al. 2022, *A&A*, **658**, A194

Powell, D., Feinstein, A. D., Lee, E. K. H., et al. 2024, *Nature*, **626**, 979

Pozuelos, F. J., Suárez, J. C., de Elía, G. C., et al. 2020, *A&A*, **641**, A23

Pozuelos, F. J., Timmermans, M., Rackham, B. V., et al. 2023, *A&A*, **672**, A70

Price, K., Storn, R., & Lampinen, J. 2005, *Differential Evolution* (Berlin: Springer)

Rayner, J. T., Toomey, D. W., Onaka, P. M., et al. 2003, *PASP*, **115**, 362

Reid, I. N., Hawley, S. L., & Gizis, J. E. 1995, *AJ*, **110**, 1838

Rein, H., & Liu, S.-F. 2012, *A&A*, **537**, A128

Rein, H., & Spiegel, D. S. 2015, *MNRAS*, **446**, 1424

Rein, H., & Tamayo, D. 2015, *MNRAS*, **452**, 376

Ricker, G. R., Winn, J. N., Vanderspek, R., et al. 2015, *J. Astron. Telesc. Instrum. Syst.*, **1**, 014003

Riddick, F. C., Roche, P. F., & Lucas, P. W. 2007, *MNRAS*, **381**, 1067

Rojas-Ayala, B., Covey, K. R., Muirhead, P. S., & Lloyd, J. P. 2012, *ApJ*, **748**, 93

Savel, A. B., Dressing, C. D., Hirsch, L. A., et al. 2020, *AJ*, **160**, 287

Savel, A. B., Hirsch, L. A., Gill, H., Dressing, C. D., & Ciardi, D. R. 2022, *PASP*, **134**, 124501

Scuflaire, R., Théado, S., Montalbán, J., et al. 2008, *Ap&SS*, **316**, 83

Sebastian, D., Gillon, M., Ducrot, E., et al. 2021, *A&A*, **645**, A100

Seifahrt, A., Stürmer, J., Bean, J. L., & Schwab, C. 2018, *SPIE Conf. Ser.*, **10702**, 107026D

Seifahrt, A., Bean, J. L., Kasper, D., et al. 2022, *SPIE Conf. Ser.*, **12184**, 121841G

Skrutskie, M. F., Cutri, R. M., Stiening, R., et al. 2006, *AJ*, **131**, 1163

Smith, J. C., Stumpe, M. C., Van Cleve, J. E., et al. 2012, *PASP*, **124**, 1000

Southworth, J. 2011, *MNRAS*, **417**, 2166

Southworth, J., Mancini, L., Novati, S. C., et al. 2010, *MNRAS*, **408**, 1680

Southworth, J., Hinse, T. C., Dominik, M., et al. 2012, *MNRAS*, **426**, 1338

Stassun, K. G., & Torres, G. 2016, *AJ*, **152**, 180

Stassun, K. G., & Torres, G. 2021, *ApJ*, **907**, L33

Stassun, K. G., Collins, K. A., & Gaudi, B. S. 2017, *AJ*, **153**, 136

Stassun, K. G., Corsaro, E., Pepper, J. A., & Gaudi, B. S. 2018a, *ApJ*, **155**, 22

Stassun, K. G., Oelkers, R. J., Pepper, J., et al. 2018b, *ApJ*, **156**, 102

Stolker, T., Quanz, S. P., Todorov, K. O., et al. 2020, *A&A*, **635**, A182

Storn, R. 1997, *J. Global Optim.*, **11**, 341

Stumpe, M. C., Smith, J. C., Van Cleve, J. E., et al. 2012, *PASP*, **124**, 985

Stumpe, M. C., Smith, J. C., Catanzarite, J. H., et al. 2014, *PASP*, **126**, 100

Tamayo, D., Rein, H., Shi, P., & Hernandez, D. M. 2020, *MNRAS*, **491**, 2885

Tang, J., Bressan, A., Rosenfield, P., et al. 2014, *MNRAS*, **445**, 4287

Thorngren, D. P., Fortney, J. J., Murray-Clay, R. A., & Lopez, E. D. 2016, *ApJ*, **831**, 64

Tokovinin, A. 2018, *PASP*, **130**, 035002

Twicken, J. D., Catanzarite, J. H., Clarke, B. D., et al. 2018, *PASP*, **130**, 064502

West, A. A., Hawley, S. L., Bochanski, J. J., et al. 2008, *AJ*, **135**, 785

Yu, X., He, C., Zhang, X., et al. 2021, *Nat. Astron.*, **5**, 822

Zacharias, N., Finch, C. T., Girard, T. M., et al. 2012, *VizieR Online Data Catalog*, **I/322A**

Zechmeister, M., Reiners, A., Amado, P. J., et al. 2020, Astrophysics Source Code Library [[record ascl:1806.014](#)]

Ziegler, C., Tokovinin, A., Briceño, C., et al. 2020, *AJ*, **159**, 19

<sup>1</sup> Astrobiology Research Unit, Université de Liège, Allée du 6 Août 19C, 4000 Liège, Belgium

<sup>2</sup> Department of Earth, Atmospheric and Planetary Science, Massachusetts Institute of Technology, 77 Massachusetts Avenue, Cambridge, MA 02139, USA

<sup>3</sup> Instituto de Astrofísica de Canarias (IAC), Calle Vía Láctea s/n, 38200, La Laguna, Tenerife, Spain

<sup>4</sup> Lund Observatory, Division of Astrophysics, Department of Physics, Lund University, Box 118, 22100 Lund, Sweden

<sup>5</sup> Department of Earth Sciences, University of Hawaii at Manoa, 1680 East-West Rd, Honolulu, HI 96822, USA

<sup>6</sup> Institute for Astrophysics, University of Vienna, Türkenschanzstrasse 17, 1180 Vienna, Austria

<sup>7</sup> Department of Astronomy and Astrobiology Program, University of Washington, Box 351580, Seattle, Washington 98195, USA

<sup>8</sup> NExSS Virtual Planetary Laboratory, Box 351580, University of Washington, Seattle, Washington 98195, USA

<sup>9</sup> Departamento de Astrofísica, Universidad de La Laguna (ULL), E-38206 La Laguna, Tenerife, Spain

<sup>10</sup> Instituto de Astrofísica de Andalucía (IAA-CSIC), Glorieta de la Astronomía s/n, 18008 Granada, Spain

<sup>11</sup> INAF- Palermo Astronomical Observatory, Piazza del Parlamento, 1, 90134 Palermo, Italy

<sup>12</sup> Komaba Institute for Science, The University of Tokyo, 3-8-1 Komaba, Meguro, Tokyo 153-8902, Japan

<sup>13</sup> Astrobiology Center, 2-21-1 Osawa, Mitaka, Tokyo 181-8588, Japan

<sup>14</sup> Research Institute for Advanced Computer Science, Universities Space Research Association, Washington, DC 20024, USA

<sup>15</sup> Institute for Particle Physics and Astrophysics, ETH Zürich, OttoStern-Weg 5, 8093 Zürich, Switzerland

<sup>16</sup> Department of Astrophysics, University of Zürich, Winterthurerstrasse 190 8057 Zürich, Switzerland

<sup>17</sup> Department of Astronomy & Astrophysics, University of Chicago, Chicago, IL, USA

<sup>18</sup> Department of Physics and Kavli Institute for Astrophysics and Space Research, Massachusetts Institute of Technology, Cambridge, MA 02139, USA

<sup>19</sup> Space Sciences, Technologies and Astrophysics Research (STAR) Institute, Université de Liège, Allée du 6 Août 19C, B-4000 Liège, Belgium

<sup>20</sup> Instituto de Alta Investigación, Universidad de Tarapacá, Casilla 7D, Arica, Chile

<sup>21</sup> Gemini Observatory/NSF NOIRLab, 670 N. A'ohoku Place, Hilo, HI 96720, USA

<sup>22</sup> Departamento de Ingeniería Topográfica y Cartografía, E.T.S.I. en Topografía, Geodesia y Cartografía, Universidad Politécnica de Madrid, 28031 Madrid, Spain

<sup>23</sup> Subaru Telescope, National Astronomical Observatory of Japan, 650 North A'ohoku Place, Hilo, HI 96720, USA

<sup>24</sup> Hamburger Sternwarte, Gojenbergsweg 112, 21029 Hamburg, Germany

<sup>25</sup> Oukaimeden Observatory, High Energy Physics and Astrophysics Laboratory, Faculty of sciences Semlalia, Cadi Ayyad University, Marrakech, Morocco

<sup>26</sup> Center for Astrophysics | Harvard & Smithsonian, 60 Garden Street, Cambridge, MA 02138, USA

<sup>27</sup> Kavli Institute for Particle Astrophysics & Cosmology, Stanford University, Stanford, CA 94305, USA

<sup>28</sup> Department of Astronomy, California Institute of Technology, Pasadena, CA 91125, USA

<sup>29</sup> Department of Astronomy & Space Sciences, Faculty of Science, Ankara University, 06100 Ankara, Türkiye

<sup>30</sup> Ankara University, Astronomy and Space Sciences Research and Application Center (Kreiken Observatory), Incek Blvd., 06837 Ahlatlıbel, Ankara, Türkiye

<sup>31</sup> AIM, CEA, CNRS, Université Paris-Saclay, Université de Paris, 91191 Gif-sur-Yvette, France

<sup>32</sup> School of Physics & Astronomy, University of Birmingham, Edgbaston, Birmingham B15 2TT, UK

<sup>33</sup> Center for Astrophysics and Space Sciences, UC San Diego, UCSD Mail Code 0424, 9500 Gilman Drive, La Jolla, CA 92093-0424, USA

<sup>34</sup> American Association of Variable Star Observers, 185 Alewife Brook Parkway, Suite 410, Cambridge, MA 02138, USA

<sup>35</sup> George Mason University, 4400 University Drive, Fairfax, VA 22030, USA

<sup>36</sup> Department of Astronomy, University of California Berkeley, Berkeley, CA 94720, USA

<sup>37</sup> Department of Multi-Disciplinary Sciences, Graduate School of Arts and Sciences, The University of Tokyo, 3-8-1 Komaba, Meguro, Tokyo 153-8902, Japan

<sup>38</sup> Dpto. Física Teórica y del Cosmos, Universidad de Granada, 18071 Granada, Spain

<sup>39</sup> Center for Space and Habitability, University of Bern, Gesellschaftsstrasse 6, 3012 Bern, Switzerland

<sup>40</sup> Center for Computational Astrophysics, Flatiron Institute, 162 Fifth Avenue, New York, NY 10010, USA

<sup>41</sup> Universidad Nacional Autónoma de México, Instituto de Astronomía, AP 70-264, Ciudad de México 04510, Mexico

<sup>42</sup> European Space Agency (ESA), European Space Research and Technology Centre (ESTEC), Keplerlaan 1, 2201 AZ Noordwijk, The Netherlands

<sup>43</sup> SUPA Physics and Astronomy, University of St. Andrews, Fife, KY16 9SS Scotland, UK

<sup>44</sup> Cavendish Laboratory, JJ Thomson Avenue, Cambridge CB3 0HE, UK

<sup>45</sup> Center for Interdisciplinary Exploration and Research in Astrophysics (CIERA), Northwestern University, 1800 Sherman, Evanston, IL 60201, USA

<sup>46</sup> Okayama Observatory, Kyoto University, 3037-5 Honjo, Kamogata-cho, Asakuchi, Okayama 719-0232, Japan

<sup>47</sup> NASA Ames Research Center, Moffett Field, CA 94035, USA

<sup>48</sup> Department of Physical Sciences, Ritsumeikan University, Kusatsu, Shiga 525-8577, Japan

<sup>49</sup> Department of Physics and Astronomy, University of Louisville, Louisville, KY 40292, USA

<sup>50</sup> Freie Universität Berlin, Institute of Geological Sciences, Malteserstr. 74-100, 12249 Berlin, Germany

<sup>51</sup> Sabadell Astronomical Society, 08206 Sabadell, Barcelona, Spain

<sup>52</sup> Europlanet Society, Department of Planetary Atmospheres of the Royal Belgian Institute for Space Aeronomy, B-1180 Brussels, Belgium

<sup>53</sup> National Astronomical Observatory of Japan, 2-21-1 Osawa, Mitaka, Tokyo 181-8588, Japan

<sup>54</sup> Astronomical Science Program, Graduate University for Advanced Studies, SOKENDAI, 2-21-1, Osawa, Mitaka, Tokyo, 181-8588, Japan

<sup>55</sup> Department of Physics, University of Rome "Tor Vergata", Via della Ricerca Scientifica 1, 00133, Rome, Italy

<sup>56</sup> INAF – Astrophysical Observatory of Turin, via Osservatorio 20, 10025, Pino Torinese, Italy

<sup>57</sup> Max Planck Institute for Astronomy, Königstuhl 17, 69117, Heidelberg, Germany

<sup>58</sup> Villa '39 Observatory, Landers, CA 92285, USA

<sup>59</sup> Wild Boar Remote Observatory, San Casciano in val di Pesa, Firenze 50026, Italy

<sup>60</sup> Institute for Particle Physics and Astrophysics, ETH Zürich, Wolfgang-Pauli-Strasse 2, 8093 Zürich, Switzerland

<sup>61</sup> Department of Physics, Aristotle University of Thessaloniki, University Campus, Thessaloniki 54124, Greece

<sup>62</sup> Department of Astronomy, University of Maryland, College Park, College Park, MD 20742, USA

<sup>63</sup> 7 Skies Observatory, Cypress County, Alberta, RASC (Royal Astronomical Society of Canada), Canada

<sup>64</sup> South African Astronomical Observatory, PO Box 9, Observatory, Cape Town 7935, South Africa

<sup>65</sup> Astrophysics Group, Keele University, Staffordshire ST5 5BG, UK

<sup>66</sup> INAF – Osservatorio Astronomico di Padova, Vicolo dell'Osservatorio 5, 35122 Padova, Italy

<sup>67</sup> Anton Pannekoek Institute for Astronomy, University of Amsterdam, Science Park 904, 1098 XH Amsterdam, The Netherlands

<sup>68</sup> Landessternwarte, Zentrum für Astronomie der Universität Heidelberg, Königstuhl 12, 69117 Heidelberg, Germany

<sup>69</sup> Kotizarovci Observatory, Sarsoni 90, 51216 Viskovo, Croatia

<sup>70</sup> Institute of Astronomy and Astrophysics, Academia Sinica, PO Box 23-141, Taipei 10617, Taiwan, ROC

<sup>71</sup> Department of Astrophysics, National Taiwan University, Taipei 10617, Taiwan, ROC

<sup>72</sup> Department of Physics & Astronomy, Johns Hopkins University, 3400 N. Charles Street, Baltimore, MD 21218, USA

<sup>73</sup> Department of Physics and Astronomy, Union College, 807 Union St., Schenectady, NY 12308, USA

<sup>74</sup> Department of Astrophysical Sciences, Princeton University, Princeton, NJ 08544, USA

<sup>75</sup> Department of Physics, Engineering and Astronomy, Stephen F. Austin State University, 1936 North St, Nacogdoches, TX 75962, USA

## Appendix A: Acknowledgments

The postdoctoral fellowship of KB is funded by F.R.S.-FNRS grant T.0109.20 and by the Francqui Foundation. MG and EJ are F.R.S.-FNRS Research Directors. This publication benefits from the support of the French Community of Belgium in the context of the FRIA Doctoral Grant awarded to MT. Funding for the TESS mission is provided by NASA's Science Mission Directorate. KAC and CNW acknowledge support from the TESS mission via subaward s3449 from MIT. This paper made use of data collected by the TESS mission, obtained from the Mikulski Archive for Space Telescopes MAST data archive at the Space Telescope Science Institute (STScI). Funding for the TESS mission is provided by the NASA Explorer Program. STScI is operated by the Association of Universities for Research in Astronomy, Inc., under NASA contract NAS 5-26555. We acknowledge the use of public TESS data from pipelines at the TESS Science Office and at the TESS Science Processing Operations Center. Resources supporting this work were provided by the NASA High-End Computing (HEC) Program through the NASA Advanced Supercomputing (NAS) Division at Ames Research Center for the production of the SPOC data products. This research has made use of the Exoplanet Follow-up Observation Program (ExoFOP; DOI: 10.26134/ExoFOP5) website, which is operated by the California Institute of Technology, under contract with the National Aeronautics and Space Administration under the Exoplanet Exploration Program. J.d.W. and MIT gratefully acknowledge financial support from the Heising-Simons Foundation, Dr. and Mrs. Colin Masson and Dr. Peter A. Gilman for Artemis, the first telescope of the SPECULOOS network situated in Tenerife, Spain. The ULiege's contribution to SPECULOOS has received funding from the European Research Council under the European Union's Seventh Framework Programme (FP/2007-2013) (grant Agreement n° 336480/SPECULOOS), from the Balzan Prize and Francqui Foundations, from the Belgian Scientific Research Foundation (F.R.S.-FNRS; grant n° T.0109.20), from the University of Liege, and from the ARC grant for Concerted Research Actions financed by the Wallonia-Brussels Federation. The research leading to these results has received funding from the ARC grant for Concerted Research Actions, financed by the Wallonia-Brussels Federation. TRAPPIST is funded by the Belgian Fund for Scientific Research (Fond National de la Recherche Scientifique, FNRS) under the grant PDR T.0120.21. TRAPPIST-North is a project funded by the University of Liege (Belgium), in collaboration with Cadi Ayyad University of Marrakech (Morocco). The ULiege's contribution to SPECULOOS has received funding from the European Research Council under the European Union's Seventh Framework Programme (FP/2007-2013) (grant Agreement n° 336480/SPECULOOS), from the Balzan Prize and Francqui Foundations, from the Belgian Scientific Research Foundation (F.R.S.-FNRS; grant n° T.0109.20), from the University of Liege, and from the ARC grant for Concerted Research Actions financed by the Wallonia-Brussels Federation. This work is supported by a grant from the Simons Foundation (PI Queloz, grant number 327127). J.d.W. and MIT gratefully acknowledge financial support from the Heising-Simons Foundation, Dr. and Mrs. Colin Masson and Dr. Peter A. Gilman for Artemis, the first telescope of the SPECULOOS network situated in Tenerife, Spain. This work is supported by the Swiss National Science Foundation (PP00P2-163967, PP00P2-190080 and the National Centre for Competence in Research PlanetS). This work has received fund from the European Research Council (ERC) under the European Union's Horizon 2020 research and innovation programme (grant agreement n° 803193/BEBOP), from the MERAC foundation, and from the Science and Technology Facilities Council (STFC; grant n° ST/S00193X/1). This work is based upon observations carried out at the Observatorio Astronómico Nacional on the Sierra de San Pedro Mártir (OAN-SPM), Baja California, México. SAINT-EX observations and team were supported by the Swiss National Science Foundation (PP00P2-163967 and PP00P2-190080), the Centre for Space and Habitability (CSH) of the University of Bern, the National Centre for Competence in Research PlanetS, supported by the Swiss National Science Foundation (SNSF). Author F.J.P, P.J.A, A.S. and A.P.T. acknowledge financial support from the Severo Ochoa grant CEX2021-001131-S funded by MCIN/AEI/10.13039/501100011033 and Ministerio de Ciencia e Innovación through the project PID2022-137241NB-C43. Partially based on observations made at the Observatorio de Sierra Nevada (OSN), operated by the Instituto de Astrofísica de Andalucía (IAA-CSIC). This work makes use of observations from the LCOGT network. Part of the LCOGT telescope time was granted by NOIRLab through the Mid-Scale Innovations Program (MSIP). MSIP is funded by NSF. This work is partly supported by JSPS KAKENHI Grant Number JP21K13955, JP24H00017, JP24H00248, JP24K00689, JP24K17082 and JP24K17083, JSPS Grant-in-Aid for JSPS Fellows Grant Number JP24KJ0241, Astrobiology Center SATELLITE Research project AB022006, JSPS Bilateral Program Number JPJSBP120249910 and JST SPRING, Grant Number JPMJSP2108. This article is based on observations made with the MuSCAT2 instrument, developed by ABC, at Telescopio Carlos Sánchez operated on the island of Tenerife by the IAC in the Spanish Observatorio del Teide. This paper is based on observations made with the MuSCAT3 instrument, developed by the Astrobiology Center and under financial supports by JSPS KAKENHI (JP18H05439) and JST PRESTO (JPMJPR1775), at Faulkes Telescope North on Maui, HI, operated by the Las Cumbres Observatory. We thank Türkiye National Observatories for the partial support in using T100 telescope with the project number 22BT100-1958. Visiting Astronomer at the Infrared Telescope Facility, which is operated by the University of Hawaii under contract 80HQTR24DA010 with the National Aeronautics and Space Administration. L.M. acknowledges financial contribution from PRIN MUR 2022 project 2022J4H55R. B.V.R. thanks the Heising-Simons Foundation for Support. This material is based upon work supported by the National Aeronautics and Space Administration under Agreement No. 80NSSC21K0593 for the program "Alien Earths". The results reported herein benefited from collaborations and/or information exchange within NASA's Nexus for Exoplanet System Science (NExSS) research coordination network sponsored by NASA's Science Mission Directorate. BR-A acknowledges funding support ANID Basal project FB210003. Support for this work was provided by NASA through the NASA Hubble Fellowship grant #HST-HF2-51559.001-A awarded by the Space Telescope Science Institute, which is operated by the Association of Universities for Research in Astronomy, Inc., for NASA, under contract NAS5-26555. VVG is a F.R.S.-FNRS Research Associate. Y.G.M.C acknowledges support from UNAM PAPIIT-IG101224. DR was supported by NASA under award number NNA16BD14C for NASA Academic Mission Services. We acknowledge financial support from the Agencia Estatal de Investigación of the Ministerio de Ciencia e Innovación MCIN/AEI/10.13039/501100011033 and the ERDF "A way of making Europe" through project PID2021-125627OB-C32, and from the Centre of Excellence "Severo Ochoa" award to the Instituto de Astrofísica de Canarias. M.S. acknowledges the support of the Italian National Institute of Astrophysics (INAF) through the project 'The HOT-ATMOS Project: characterizing the atmospheres of hot giant planets as a key to understand the exoplanet diversity' (1.05.01.85.04). E.E-B. acknowledges financial support from the European Union and the State Agency of Investigation of the Spanish Ministry of Science and Innovation (MICINN) under the grant PRE2020-093107 of the Pre-Doc Program for the Training of Doctors (FPI-SO) through FSE funds. J.S. acknowledges support from STFC under grant number ST/Y002563/1.

## Appendix B: TESS observations log for TOI-2015

Table B.1: TESS observations log for TOI-2015.

Sector	Camera	CCD	Observation date
24	1	4	2020 April 16 – May 13
51	2	2	2022 April 22 – May 18
78	1	3	2024 April 23 – May 21

## Appendix C: Ground-based observations log for TOI-2015 b

Table C.1: Ground-based observations log for TOI-2015 b: Telescope, size, observation date and filter.

Observatory	Aperture [m]	Date (UT)	Filter	Coverage
LCO-SAAO	1.0	2020.07.05	Sloan- $i'$	Ingress
MuSCAT3	2.0	2021.06.12	Sloan- $g', r', i', z_s$	Full
MuSCAT3	2.0	2021.07.28	Sloan- $g', r', i', z_s$	Full
LCO-CTIO	1.0	2021.08.04	Sloan- $i'$	Egress
MuSCAT3	2.0	2022.03.26	Sloan- $i', z_s$	Full
MuSCAT3	2.0	2022.04.05	Sloan- $i', z_s$	Ingress
MuSCAT	1.88	2022.05.06	Sloan- $r', z_s$	Full
SPECULOOS-North	1.0	2022.05.19	$I + z'$	Full
MuSCAT2	1.5	2022.05.19	Sloan- $g', r', i', z_s$	Full
MuSCAT3	2.0	2022.05.22	Sloan- $r', i', z_s$	Full
SPECULOOS-North	1.0	2022.05.29	$I + z'$	Full
MuSCAT2	1.5	2022.05.29	Sloan- $g', r', i', z_s$	Full
TRAPPIST-South	0.6	2022.06.09	$I + z'$	Full
SPECULOOS-North	1.0	2022.06.19	$I + z'$	Full
SAINT-EX	1.0	2022.06.19	$I + z'$	Full
SPECULOOS-North	1.0	2022.06.25	$I + z'$	Egress
OSN	1.5	2022.06.25	$Ic$	Egress
SPECULOOS-North	1.0	2022.07.15	$I + z'$	Full
SPECULOOS-North	1.0	2022.07.25	$I + z'$	Full
SPECULOOS-North	1.0	2022.08.04	$I + z'$	Ingress
LCO-Teid	1.0	2022.08.04	Sloan- $i'$	Ingress
SPECULOOS-North	1.0	2023.04.02	$I + z'$	Full
TRAPPIST-North	1.0	2023.04.02	$I + z'$	Full + Flip
SPECULOOS-North	1.0	2023.04.12	$I + z'$	Ingress
LCO-CTIO	1.0	2023.04.12	Sloan- $i'$	Full
LCO-McD	1.0	2023.04.12	Sloan- $i'$	Full
LCO-McD	1.0	2023.04.12	Sloan- $i'$	Full
MuSCAT3	2.0	2023.04.15	Sloan- $g', r', i', z_s$	Full
LCO-CTIO	1.0	2023.04.23	Sloan- $i'$	Full
LCO-SSO	1.0	2023.04.26	Sloan- $i'$	Ingress
TRAPPIST-North	1.0	2023.04.29	$I + z'$	Full + thin clouds *
TRAPPIST-North	1.0	2023.05.09	$I + z'$	Full + Flip
SPECULOOS-North	1.0	2023.05.09	$I + z'$	Full
LCO-Teid	1.0	2023.05.09	Sloan- $i'$	Full
IAC80	1.0	2023.05.09	Sloan- $r'$	Full *
LCO-HAL	0.4	2023.05.12	Sloan- $i'$	Full
SPECULOOS-North	1.0	2023.05.19	$I + z'$	Full
LCO-Teid	1.0	2023.05.19	Sloan- $i'$	Full
SPECULOOS-North	1.0	2023.05.29	$I + z'$	Full
LCO-Teid	1.0	2023.05.29	Sloan- $i'$	Full
LCO-CTIO	1.0	2023.05.29	Sloan- $i'$	Full
LCO-CTIO	1.0	2023.06.08	Sloan- $i'$	Full
SPECULOOS-North	1.0	2023.06.15	$I + z'$	Egress
CAHA-1.23m	1.23	2023.06.15	GG-495	Full
SPECULOOS-North	1.0	2023.06.25	$I + z'$	Full
LCO-Teid	1.0	2023.06.25	$i'$	Full
TUBITAK-1m0	1.0	2023.06.25	Clear	Full
LCO-McD	1.0	2023.06.29	Sloan- $i'$	Full
SPECULOOS-North	1.0	2023.07.05	$I + z'$	Full
MuSCAT3	2.0	2024.03.19	Sloan- $g', r', i', z_s$	Ingress
LCO-CTIO	1.0	2024.03.26	Sloan- $i'$	Full
SPECULOOS-North	1.0	2024.04.02	$I + z'$	Full
MuSCAT3	2.0	2024.04.05	Sloan- $i', z_s$	Full

**Notes.** \* designs the transits that we excluded in our photodynamical analysis due to the low SNR.

## Appendix D: Mid-transit timings measured for TOI-2015 b

Table D.1: Mid-transit timings measured for TOI-2015 b in this work.

Epoch	Transit mid-time (BJD <sub>TDB</sub> )	Telescope(s)
-226	2458956.03370946 ± 0.00311000	TESS
-225	2458959.37366368 ± 0.00517000	TESS
-224	2458962.72816271 ± 0.00549000	TESS
-223	2458966.07238390 ± 0.00337000	TESS
-222	2458969.41420846 ± 0.00285000	TESS
-221	2458972.76329561 ± 0.00335000	TESS
-220	2458976.11441643 ± 0.00640000	TESS
-219	2458979.45588928 ± 0.00344000	TESS
-202	2459036.39117005 ± 0.00071500	LCOGT-1m0
-100	2459377.94893691 ± 0.00860149	MuSCAT3
-86	2459424.78535186 ± 0.00373972	MuSCAT3
-84	2459431.48034340 ± 0.00059700	LCOGT-1m0
-14	2459666.06899834 ± 0.00014800	MuSCAT3
-11	2459676.12237684 ± 0.00370000	MuSCAT3
-4	2459699.53654669 ± 0.00463000	TESS
-2	2459706.23337622 ± 0.00048800	TESS + MuSCAT
0	2459712.92259750 ± 0.00251000	TESS
1	2459716.27075880 ± 0.00178000	TESS
2	2459719.61366655 ± 0.00036900	SPECULOOS-North + MuSCAT2
3	2459722.95871120 ± 0.00014900	MuSCAT3
5	2459729.64513527 ± 0.00039600	SPECULOOS-North
8	2459739.67809341 ± 0.00063500	TRAPPIST-South
11	2459749.70844875 ± 0.00039500	SPECULOOS-North
13	2459756.38869089 ± 0.00426315	SPECULOOS-North + OSN-1.5m
16	2459766.42456143 ± 0.00031500	SAINT-EX
19	2459776.45123640 ± 0.00039400	SPECULOOS-North
22	2459786.48088223 ± 0.00039300	SPECULOOS-North
25	2459796.51408078 ± 0.00298935	SPECULOOS-North + LCOGT-1m0
97	2460037.68757200 ± 0.00031000	SPECULOOS-North + TRAPPIST-North
100	2460047.74237832 ± 0.00023400	SPECULOOS-North + LCOGT-1m0
101	2460051.09383990 ± 0.00019800	MuSCAT3
103	2460057.79748197 ± 0.00040000	LCOGT-1m0
104	2460061.14790259 ± 0.00153000	LCOGT-1m0
105	2460064.51864170 ± 0.02000000	TRAPPIST-North
108	2460074.55214637 ± 0.00031000	SPECULOOS-North + LCOGT-1m0
109	2460077.89791170 ± 0.00330000	LCOGT-0.35m
111	2460084.60438173 ± 0.00303000	SPECULOOS-North + LCOGT-1m0
114	2460094.65119102 ± 0.00024000	SPECULOOS-North + LCOGT-1m0
117	2460104.69785000 ± 0.00040000	LCOGT-1m0
119	2460111.39533000 ± 0.00020000	SPECULOOS-North + CAHA-1.23m
122	2460121.43747558 ± 0.0002400	SPECULOOS-North + LCOGT-1m0 + TUBITAK-1m0
125	2460131.47835115 ± 0.00051600	SPECULOOS-North
202	2460389.14534935 ± 0.00034517	MuSCAT3
204	2460395.84795994 ± 0.00095855	LCOGT-1m0
206	2460402.55465865 ± 0.00039847	SPECULOOS-North
207	2460405.90637088 ± 0.00024873	MuSCAT3
216	2460436.083329 ± 0.002400	TESS
217	2460439.440196 ± 0.002300	TESS
218	2460442.784055 ± 0.002300	TESS
220	2460449.479219 ± 0.001500	TESS

## Appendix E: Results for 2:1 near resonance scenario

Table E.1: Physical parameters of the TOI-2015 system for the 2:1 near-resonance scenario.

Parameter	Unit	TOI-2015 b	TOI-2015 c
Orbital period $P$	days	$3.34649323^{+0.00004513}_{-0.00004738}$	$6.698178^{+0.000195}_{-0.000131}$
Transit-timing $T_0$	BJD <sub>TDB</sub>	$2459424.78461920^{+0.00019598}_{-0.00018066}$	–
Orbital semi-major axis $a$	au	$0.02931232 \pm 0.000003$	$0.046559 \pm 0.000005$
Impact parameter $b$	$R_\star$	$0.841^{+0.004}_{-0.004}$	$30.31^{+0.09}_{-0.14}$
Transit duration $W$	hour	$1.118 \pm 0.007$	–
eccentricity $e$	–	$0.1777^{+0.0084}_{-0.0087}$	$0.0099^{+0.0044}_{-0.0033}$
$\sqrt{e} \cos(w)$	–	$-0.4136^{+0.0111}_{-0.0105}$	$0.0111^{+0.0021}_{-0.0024}$
$\sqrt{e} \sin(w)$	–	$0.0816^{+0.0087}_{-0.0092}$	$-0.099^{+0.0183}_{-0.0202}$
Mean anomaly $M$	deg	–	$6.246^{+0.022}_{-0.020}$
Orbital inclination $i$	deg	$87.87 \pm 0.01$	$28.44^{+3.03}_{-2.00}$
Radius ratio $R_p/R_\star$	$R_\star$	$0.09849^{+0.00045}_{-0.00042}$	–
Scaled semi-major axis $a/R_\star$	–	$19.2758^{+0.0064}_{-0.0056}$	$30.6220 \pm 0.0102$
Planet radius $R_p$	$R_\oplus$	$3.5119^{+0.016}_{-0.015}$	–
Planet Mass $M_p$	$M_\oplus$	$8.032^{+0.67}_{-0.44}$	$18.11^{+1.05}_{-1.08}$
Planet density $\rho_p$	g/cm <sup>3</sup>	$1.022^{+0.077}_{-0.064}$	–
Planet irradiation $S_p$	$S_\oplus$	$13.19 \pm 0.38$	$5.23 \pm 0.15$
Planet surface gravity log( $g_p$ )	–	$2.81 \pm 0.21$	–

## Appendix F: Results for 5:2 near resonance scenario

Table F.1: Physical parameters of the TOI-2015 system for the 5:2 near-resonance scenario.

Parameter	Unit	TOI-2015 b	TOI-2015 c
Orbital period $P$	days	$3.34800359^{+0.00005184}_{-0.00005563}$	$8.374068^{+0.000574}_{-0.000504}$
Transit-timing $T_0$	BJD <sub>TDB</sub>	$2459424.785375^{+0.000181}_{-0.000174}$	–
Orbital semi-major axis $a$	au	$0.029322 \pm 0.000003$	$0.0540318 \pm 0.000007$
Impact parameter $b$	$R_\star$	$0.8146^{+0.0040}_{-0.0041}$	$17.23^{+0.66}_{-0.67}$
Transit duration $W$	hour	$1.094 \pm 0.006$	–
eccentricity $e$	–	$0.324^{+0.0072}_{-0.0073}$	$0.211^{+0.006}_{-0.007}$
$\sqrt{e} \cos(w)$	–	$-0.273^{+0.014}_{-0.014}$	$0.4107^{+0.009}_{-0.009}$
$\sqrt{e} \sin(w)$	–	$-0.499^{+0.011}_{-0.011}$	$-0.207^{+0.022}_{-0.016}$
Mean anomaly $M$	deg	–	$2.422^{+0.025}_{-0.022}$
Orbital inclination $i$	deg	$87.715 \pm 0.016$	$48.54^{+1.18}_{-1.29}$
Radius ratio $R_p/R_\star$	$R_\star$	$0.09756^{+0.00042}_{-0.00040}$	–
Scaled semi-major axis $a/R_\star$	–	$19.2826^{+0.0062}_{-0.0060}$	$35.539 \pm 0.012$
Planet radius $R_p$	$R_\oplus$	$3.479^{+0.015}_{-0.014}$	–
Planet Mass $M_p$	$M_\oplus$	$22.12^{+0.79}_{-0.88}$	$11.61^{+0.71}_{-0.74}$
Planet density $\rho_p$	g/cm <sup>3</sup>	$2.89^{+0.11}_{-0.12}$	–
Planet irradiation $S_p$	$S_\oplus$	$13.18 \pm 0.38$	$3.88 \pm 0.11$
Planet surface gravity log( $g_p$ )	–	$3.25 \pm 0.12$	–

## Appendix G: Model parameters and priors

Table G.1: PyTTV model parameters and priors.

Description	Units	Prior
<i>Stellar parameters</i>		
Stellar mass	$[M_\odot]$	$\mathcal{N}(0.33, 0.02)$
Stellar radius	$[R_\odot]$	$\mathcal{N}(0.339, 0.016)$
Limb darkening $q_1^a$	[ $\cdot$ ]	$\mathcal{U}(0, 1)$
Limb darkening $q_2^a$	[ $\cdot$ ]	$\mathcal{U}(0, 1)$
<i>Planet b parameters</i>		
$\log_{10}$ mass	$[\log_{10} M_\odot]$	$\mathcal{N}(-4.8, 0.1)^b$
Radius ratio	$[R_\star]$	$\mathcal{N}(0.1, 0.01)$
Transit centre	$[\text{BJD}_{\text{TDB}}]$	$\mathcal{N}(2459712.930, 0.005)$
Orbital period	[d]	$\mathcal{N}(3.35, 0.01)$
Impact parameter	$[R_\star]$	$\mathcal{U}(0.5, 1.0)$
$\sqrt{e} \cos \omega$	[ $\cdot$ ]	$\mathcal{U}(-0.25, 0.25)$
$\sqrt{e} \sin \omega$	[ $\cdot$ ]	$\mathcal{U}(-0.25, 0.25)$
$\Omega$	[rad]	$\mathcal{N}(\pi, 0.0001)$
<i>Planet c parameters</i>		
$\log_{10}$ mass	$[\log_{10} M_\odot]$	$\mathcal{U}(-4.4, 0.1)^b$
Radius ratio	$[R_\star]$	$\mathcal{N}(0.1, 0.01)$
Mean anomaly at $T_{\text{ref}}$	[rad]	$\mathcal{U}(0, 2\pi)$
Orbital period	[d]	Depends on the scenario
Impact parameter	$[R_\star]$	$\mathcal{N}(0.0, 3.0)$
$\sqrt{e} \cos \omega$	[ $\cdot$ ]	$\mathcal{U}(-0.25, 0.25)$
$\sqrt{e} \sin \omega$	[ $\cdot$ ]	$\mathcal{U}(-0.25, 0.25)$
$\Omega$	[rad]	$\mathcal{N}(\pi, 0.0001)$
<i>RV parameters</i>		
Linear trend	[m/s/d]	$\mathcal{N}(0, 1.0)$
Systemic velocity 1	[m/s]	$\mathcal{N}(-25855, 200)$
Systemic velocity 2	[m/s]	$\mathcal{N}(-25416, 200)$
$\log_{10}$ jitter 1	$[\log_{10} \text{m/s}]$	$\mathcal{N}(-1, 0.1)$
$\log_{10}$ jitter 2	$[\log_{10} \text{m/s}]$	$\mathcal{N}(-1, 0.1)$

**Notes.** All the planetary parameters except the radius ratio and  $\log_{10}$  mass are defined at a reference time,  $t_{\text{ref}} = 2459424.785$ .

<sup>(a)</sup>We use the triangular parameterization for quadratic limb darkening introduced by Kipping (2013). <sup>(b)</sup>The  $\log_{10}$  planet mass priors are loosely based on two-planet RV analysis.

## Appendix H: Posterior probability distribution for TOI-2015 for the 5:3 scenario.

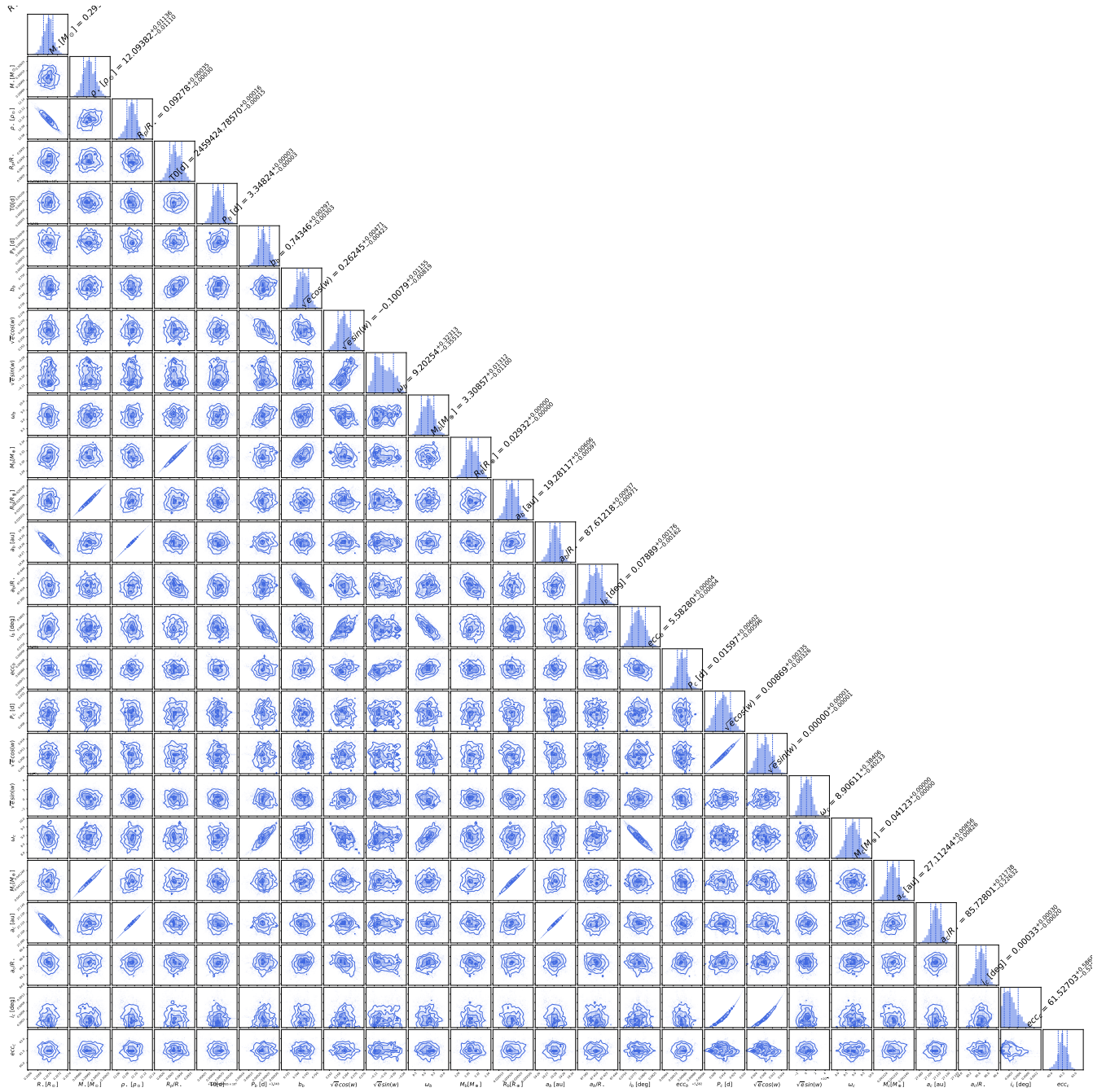


Fig. H.1: Corner plot of the posterior probability distribution from the PyTTV analysis for the parameters of the host star for the 5:3 scenario.